



Disentangling the AGN and Star formation Contributions to the Radio–X-Ray Emission of Radio-loud Quasars at $1 < z < 2$

Mojegan Azadi¹, Belinda Wilkes¹, Joanna Kuraszkiewicz¹, Jonathan McDowell¹, Ralf Siebenmorgen²,
Matthew Ashby¹, Mark Birkinshaw³, Diana Worrall³, Natasha Abrams⁴, Peter Barthel⁵, Giovanni G. Fazio¹,

Martin Haas⁶, Sóley Hyman⁷, Rafael Martínez-Galarza¹, and Eileen T. Meyer⁸

¹ Center for Astrophysics | Harvard & Smithsonian, 60 Garden Street, Cambridge, MA, 02138, USA; mojegan.azadi@cfa.harvard.edu

² European Southern Observatory, Karl-Schwarzschild-Str. 2, D-85748 Garching b. München, Germany

³ H.H. Wills Physics Laboratory, University of Bristol, UK

⁴ Astronomy Department, University of California at Berkeley, Berkeley, CA 94720, USA

⁵ Kapteyn Institute, University of Groningen, The Netherlands

⁶ Astronomisches Institut, Ruhr-University, Bochum, Germany

⁷ Steward Observatory, University of Arizona, 933 North Cherry Avenue, Tucson, AZ, 85721, USA

⁸ Department of Physics, University of Maryland Baltimore County, Baltimore, MD, 21250, USA

Received 2020 November 9; revised 2023 January 20; accepted 2023 February 6; published 2023 March 16

Abstract

We constrain the emission mechanisms responsible for the prodigious electromagnetic output generated by active galactic nuclei (AGNs) and their host galaxies with a novel state-of-the-art AGN radio-to-X-ray spectral energy distribution model fitting code (ARXSED). ARXSED combines multiple components to fit the spectral energy distributions (SEDs) of AGNs and their host galaxies. Emission components include radio structures such as lobes and jets, infrared emission from the AGN torus, visible-to-X-ray emission from the accretion disk, and radio-to-ultraviolet emission from the host galaxy. Applying ARXSED to the radio SEDs of 20 3CRR quasars at $1 < z < 2$ verifies the need for more than a simple power law when compact radio structures are present. The nonthermal emission contributes 91%–57% of the observed-frame 1.25 mm to 850 μm flux, and this component must be accounted for when using these wavelengths to estimate star formation properties. We predict the presence of strong radio-linked X-ray emission in more than half the sample sources. ARXSED estimates median (and the associated first and third quartile ranges) BH mass of $2.9_{1.7}^{6.0} \times 10^9 M_{\odot}$, logarithm of Eddington ratio of $-1.0_{-1.2}^{-0.6}$, and spin of $0.98_{0.94}^{0.99}$ for our sample. The inferred AGN torus and accretion disk parameters agree with those estimated from spectroscopic analyses of similar samples in the literature. We present the median intrinsic SED of the luminous radio-loud quasars at $1 < z \lesssim 2$; this SED represents a significant improvement in the way each component is modeled.

Unified Astronomy Thesaurus concepts: Radio galaxies (1343); Active galactic nuclei (16); Quasars (1319); AGN host galaxies (2017); Radio loud quasars (1349); Spectral energy distribution (2129)

1. Introduction

It is now widely accepted that the center of almost every galaxy hosts a supermassive black hole (SMBH), which by accretion of gas and dust can turn into an active galactic nucleus (AGN; for a review, see Heckman & Best 2014). While there has been significant progress in our understanding of galaxy formation and evolution over the past decades (e.g., Madau & Dickinson 2014), there is as yet no coherent picture of the role AGNs play in this evolution (e.g., see Aird et al. 2012; Page et al. 2012; Rosario et al. 2012; Rovilos et al. 2012; Azadi et al. 2015; Bernhard et al. 2016; Brown et al. 2019; Shanguan et al. 2020). As both release a tremendous amount of energy over a wide range of wavelengths, it is critical to disentangle the radiation from the AGN and the host galaxy as a function of wavelength in order to understand better the emission mechanisms operating in them.

In the standard picture of a powerful active galaxy (e.g., Urry & Padovani 1995), a central SMBH is surrounded by a gaseous, optically thick, geometrically thin, accretion disk that

generates visible (O), ultraviolet (UV), and soft X-ray emission (e.g., Novikov & Thorne 1973; Shakura & Sunyaev 1976; Rees 1984). This central engine is, in turn, surrounded by an asymmetric dusty structure known as the torus, with a half-opening angle of $\sim 60^\circ$ (e.g., Willott et al. 2000; Wilkes et al. 2013). The torus absorbs some of the UV and optical photons and re-radiates them at near-infrared (NIR) to MIR-infrared (MIR) wavelengths (e.g., Neugebauer et al. 1979; Rieke & Lebofsky 1981). Radiation from the torus dominates an AGN's emission at 1–40 μm (e.g., Elvis et al. 1994; Netzer et al. 2007; Mullaney et al. 2011). A subset of AGNs ($\sim 15\%$; Kellermann et al. 1989; Urry & Padovani 1995), known as radio galaxies, also emit strongly at radio frequencies (for a recent review, see Hardcastle & Croston 2020) as a result of the interactions of relativistic electrons (or positrons) with the magnetic fields (see Ghisellini 2013, for a detailed review). Radio galaxies are designated as FR II or FR I based on their morphology: FR II sources are double-lobed and are brightest near the ends of the lobes, while FR I have the brightest extended radio emission near the center of the structure (Fanaroff & Riley 1974). As for all AGNs, radio galaxies are classified as broad-line (Type 1) or narrow-line (Type 2) depending on the presence/absence of broad UVOIR emission lines, which is a function of viewing angle. The present work focuses on a sample of broad-line

radio galaxies having FR II morphology and high power that are classified as quasars.

Below, we briefly describe the major AGN components according to a selective survey of the recent literature. The elements considered include the AGN accretion disk, the torus, and the radio structures. Our radio-to-X-ray spectral energy distribution model fitting code (ARXSED) accounts for the emission from all of these elements.

The accretion disk: since the classical models of Novikov & Thorne (1973) and Shakura & Sunyaev (1976), there have been many attempts to model the emission from the accretion disk (e.g., Done et al. 2012, 2013; Petrucci et al. 2013; Kubota & Done 2018, among others). Generally, the temperature and optical depth of the gas in the disk are inversely related to distance from the SMBH. The temperature gradient results in an energy gradient in the emission, with hard X-rays (>2 keV) originating in the inner region while UV and visible radiation originate in the outer disk (e.g., Done et al. 2012; Kubota & Done 2018). The hard X-ray radiation is due to the Compton up-scattering of the accretion disk photons in a hot (electron temperatures ~ 100 keV) and optically thin corona located above and below the inner disk (e.g., Haardt & Maraschi 1993; Svensson & Zdziarski 1994; Petrucci et al. 2001). The hard X-ray emission is usually consistent with a simple power-law spectrum. At lower energies (~ 2 keV), many AGNs show a soft X-ray excess above the extension of the harder power law (e.g., Gierliński & Done 2004; Piconcelli et al. 2005; Bianchi et al. 2009). There is no single, widely accepted origin for the soft excess (e.g., Czerny et al. 2003; Crummy et al. 2006; Petrucci et al. 2018). In this study, we adopt the accretion disk model of Kubota & Done (2018), which assumes that the soft X-ray excess results from Comptonization of thermal photons by a warm ($kT_e \sim 0.1$ – 1 keV), optically thick ($\tau \sim 10$ – 25) layer above the surface of the disk (also see Czerny et al. 2003; Kubota & Done 2018; Petrucci et al. 2018). In this model, the total radiative power of the accretion disk depends on the black hole mass, the mass accretion rate, the spin of the SMBH, and the radial dependence of the optical depth (e.g., Davis & Laor 2011; Done et al. 2012; Kubota & Done 2018).

The torus: the distribution of dust in the torus has been the subject of many studies. Early studies proposed a homogeneous structure in which the dust is smoothly distributed in a toroidal disk (e.g., Pier & Krolik 1992; Efstathiou & Rowan-Robinson 1995; Fritz et al. 2006). However, these models are not able to describe some of the observed features; for example, the $9.7 \mu\text{m}$ silicate absorption feature in Type 1 sources (e.g., Roche et al. 1991). A significant part of the MIR radiation comes from the polar regions (e.g., Braatz et al. 1993; Hönig et al. 2013), which toroidal models could not explain. A clumpy circumnuclear torus was then put forward as a possible solution (e.g., Nenkova et al. 2008; Hönig & Kishimoto 2010; Hönig et al. 2013). Recently, Siebenmorgen et al. (2015) proposed a model in which the dust can be distributed in a homogeneous disk, a clumpy medium, or a combination of both (Siebenmorgen et al. 2005; Feltre et al. 2012). The Siebenmorgen et al. (2015) model reproduces the MIR spectra of AGNs, including the $9.7 \mu\text{m}$ silicate absorption feature in Type 1 AGNs, the radiation from the hot dust close to the sublimation temperature, and the MIR radiation from the ionization cone (e.g., Braatz et al. 1993; Cameron et al. 1993; Hönig et al. 2013). ARXSED incorporates the Siebenmorgen et al. (2015) torus model.

The radio structures: the radio-loud AGNs launch powerful jets that persist as highly collimated structures until they terminate as bright shocks (“hot spots”) at the interface with the circumgalactic or intergalactic medium (IGM). The observed shape of the radio spectra depends on the age and acceleration of the electron population, and viewing angle, among other factors. In a simplified picture, the radio spectrum of a lobe-dominated AGN can be described with a power law ($L_\nu \propto \nu^\alpha$). However, in AGNs with compact radio structures such as radio cores and hot spots, superposition of various components makes the shape of the spectrum more complex. Therefore, to model the radio emission, multicomponent models with different spectral indices are required. The radiation from these structures eventually breaks at high frequencies as a result of synchrotron radiation losses and terminates at a cutoff frequency due to a drop in the electron population caused by rapid energy losses (e.g., Blandford & Königl 1979; Königl 1981).

What sparks the radio-loud phase in some AGNs is still unknown and may be stochastic by nature. Some studies find that the triggering mechanism of the radio-loud phase is intrinsic to the AGN rather than the host galaxies or the environments (e.g., Kellermann et al. 2016; Coziol et al. 2017), while others find cold star-forming gas in galaxies (e.g., Best & Heckman 2012; Janssen et al. 2012) or the brightness of the cluster and density of the environment they live in (e.g., Burns 1990; Best et al. 2007) increase the likelihood of hosting a radio-loud AGN. The prevalence of radio-loud AGNs and the power of their radio emission (i.e., $L_{1.4 \text{ GHz}}$) correlates strongly with the intrinsic properties of the SMBH (e.g., SMBH mass; Best et al. 2005; Coziol et al. 2017). Some studies suggest that the BH mass is a critical parameter in dividing the radio-loud and radio-quiet populations (e.g., Chiaberge & Marconi 2011). There is as yet no consensus on whether the Eddington ratio (which is the ratio of the bolometric luminosity to the Eddington luminosity)

$$\begin{aligned} \lambda_{\text{Edd}} &= L_{\text{bol}}/L_{\text{Edd}} \\ L_{\text{Edd}} &\propto M_{\text{BH}} \end{aligned} \quad (1)$$

and/or spin have a role in triggering the radio-loud phase (e.g., Sikora et al. 2007; Chiaberge & Marconi 2011; Coziol et al. 2017).

The multiple components described above emit radiation covering 10 decades of frequency from X-ray to radio. To constrain these components, we, therefore, need observations across a broad range of wavelengths. However, obtaining a multiwavelength data set is very challenging, and in the case of quasars, variability adds more complications. Over the past three decades, numerous studies have focused on spectral energy distribution (SED) analysis of AGN populations (e.g., Edelson & Malkan 1986; Elvis et al. 1994; Richards et al. 2006; Shang et al. 2011; Elvis et al. 2012; Hao et al. 2014). A number of these studies have attempted to understand whether quasars’ behavior can be described with an average SED. Elvis et al. (1994) presented the first high-quality broad (X-ray to radio) atlas of quasar SEDs at $z \lesssim 1$ using then-current telescopes such as Einstein, the International Ultraviolet Explorer, and the Infrared Astronomical Satellite (IRAS). Elvis et al. (1994) presented median SEDs for the radio-loud and radio-quiet quasars that have been extensively used and overall work remarkably well in the 0.1 – $1 \mu\text{m}$ wavelength range for

AGNs of various luminosities and Eddington ratios (Elvis 2010). However, there is a large dispersion around their median SED, which can reflect on the inferred properties of the quasars. Additionally, their sample is not representative of the overall quasar population and is biased toward X-ray bright and blue quasars (e.g., Jester 2005; Shang et al. 2011).

The average SED of quasars has been investigated by others in a similarly broad range of the spectrum, radio-to-X-ray, (e.g., Richards et al. 2006; Shang et al. 2011; Elvis et al. 2012) or a more limited range (e.g., Kuraszek et al. 2003; Polletta et al. 2007; Mullaney et al. 2011; Lani et al. 2017, among others) using more recent spectroscopic and photometric data. Richards et al. (2006) found a wide range of SED shapes for quasars and concluded that assuming an average SED can potentially lead to 50% errors in the bolometric luminosity estimate. Hao et al. (2014) found that in X-ray selected, radio-quiet quasars, the average SED has no significant dependence on redshift, bolometric luminosity, SMBH mass, or Eddington ratio, while others (e.g., Geach et al. 2011; Kirkpatrick et al. 2017) found that local quasar templates may not be applicable to AGNs at higher redshifts. One of the many challenges in AGN SED analysis is the contamination of the broadband photometry by the host galaxy. Most of the studies noted here use scaling relations such as $M_{\text{BH}} - \sigma$ (e.g., Hunt 2003) or $L_{\text{host}} - L_{\text{AGN}}$ (Vanden Berk et al. 2006) or color-color diagnostics (e.g., Grewing et al. 1968; Sandage 1971) to estimate the host galaxy contamination. However, each of these scaling relations has large uncertainties that significantly affect the SED.

With the wealth of information stored in the photometric data obtained with modern telescopes with higher sensitivity and resolution, many studies have moved toward fitting complex models to the broadband photometry that can describe the radiation from the AGN and the host galaxy simultaneously and provide estimates of the physical properties of each (i.e., SMBH mass and stellar mass). The galaxy SED models (e.g., MAGPHYS: da Cunha et al. 2008; FAST: Kriek et al. 2009; CIGALE: Boquien et al. 2019) adopt libraries of galaxy templates with different stellar populations. These libraries are often built on assumptions on star formation history (SFH), initial mass function (IMF), dust attenuation law, etc., which each have their own uncertainties. In the case of active galaxies, additional templates (i.e., torus and accretion disk) are required to describe the radiation from the central engine. For instance, Berta et al. (2013) presented the SED3fit model, which combines the galaxy templates from MAGPHYS (da Cunha et al. 2008) with the torus templates of Fritz et al. (2006) to describe the radiation from the AGN and its host within 8–500 μm . Leja et al. (2018) used the galaxy SED model of Prospector- α (Leja et al. 2017) and the clumpy torus model of Nenkova et al. (2008) to fit the SED of nearby AGNs at 1–100 μm . While overall these models are successful in modeling the AGN and the host galaxy’s emission, portraying a complete picture of AGNs requires a data set that covers the radiation from the accretion disk, which is the primary source of AGN power, and the radio component (in the case of radio-loud AGNs).

The present work describes SED modeling of a subset of AGNs from the Revised-Third Cambridge Catalogue of Radio Sources (3CR; Spinrad et al. 1985). Specifically, we construct the radio to X-ray SEDs of 3CRR⁹ (Laing et al. 1983) quasars at $1 < z \lesssim 2$, which together with narrow-line radio galaxies in

the same redshift band define an orientation-independent sample of luminous AGNs. We focus on this epoch—known as Cosmic High Noon—because of its well-known significance for the growth of SMBHs and the assembly of the galaxy bulges in which they reside. SED fitting of the full IR continuum of 3CR sources at a range of redshifts indicates that orientation determines the MIR–NIR continuum shapes (e.g., Haas et al. 2008; Drouart et al. 2014; Podigachoski et al. 2015, 2016b). Here we expand on earlier SED fitting of the IR continuum to include the radio-to-X-ray emission. This paper introduces the detailed, state-of-the-art AGN Radio-X-ray SED modeling code (ARXSED) and applies it to the 3CRR quasars. We present the estimated physical properties of the AGN components derived from the modeling (e.g., SMBH mass, Eddington ratio, and spin). SED fitting of the narrow-line radio galaxies and properties of the host galaxies will be presented in future papers.

This paper is organized as follows: Section 2 describes the sample selection and the multiwavelength data used for the SED analysis. Section 3 presents the details of our SED modeling and the components used to describe the emission from the AGN and the host galaxy at different wavelengths. Section 4 describes the fitting results for individual sources, and results of the SED analysis are discussed in Section 5. We present a summary of our findings in Section 6. Throughout the paper, we adopt a flat cosmology with $\Omega_{\Lambda} = 0.7$ and $H_0 = 72 \text{ km s}^{-1} \text{ Mpc}^{-1}$.

2. Sample and Data Compilation

The 3CRR catalog (Laing et al. 1983) includes 180 FR II radio galaxies and quasars up to a redshift of 2.5 and is 100% complete to a 178 MHz flux density of 10 Jy. Of these, 38 sources are at $1 < z \lesssim 2$ (Wilkes et al. 2013) including 21 that have broad emission lines (and classified as quasars), and 17 showing only narrow emission lines. In this study, we limit our sample specifically to the quasars to ensure that the accretion disk dominates the visible-UV radiation. The sample is presented in Table 1. We have excluded the red quasar (3C 68.1) from our analysis, as its SED is similar to those of the narrow-line radio galaxies. 3C 68.1 will be discussed in a future paper.

AGNs have obscuration-dependent emission that results in strong selection effects at most wavelengths (e.g., Azadi et al. 2017). However, selection based on optically thin, low-frequency (178 MHz) radio emission uniquely finds AGNs without the orientation bias. The complete nature of the 3CRR catalog, combined with the sources’ high brightness and luminosities, freedom from orientation bias, and the availability of comprehensive multiwavelength data, makes the 3CRR sources an optimal sample to characterize the luminous radio-loud AGN population.

The radio properties of our sample, from the radio morphologies and the lengths of the radio structures (e.g., radio extents measured from lobe to lobe) to the fraction of radiation from the radio core relative to the lobes at 5 GHz (a jet orientation indicator), among many other properties, have been studied in great detail (Lonsdale & Barthel 1984; Akujor et al. 1991; Bridle et al. 1994; Akujor & Garrington 1995; Ludke et al. 1998; O’Dea 1998).

Although the 3CRR sample has been extensively studied, surprisingly, many sources miss critical data needed for estimating the basic parameters of their central engines and

⁹ The Revised-3CR (3CRR) is the most complete version of the 3CR sample that only includes extragalactic sources, with 178 MHz flux density limit $>10 \text{ Jy}$, decl. $>10^\circ$, and Galactic latitude $>10^\circ$ or $< -10^\circ$.

Table 1
The 3CRR Quasars Modeled in This Work

Name	R.A., Decl. (J2000.0)	z
3C 009	00:20:25.2, +15:40:55	2.009
3C 014	00:36:06.5, +18:37:59	1.469
3C 043	01:29:59.8, +23:38:20	1.459
3C 181	07:28:10.3, +14:37:36	1.382
3C 186	07:44:17.4, +37:53:17	1.067
3C 190	08:01:33.5, +14:14:42	1.195
3C 191	08:04:47.9, +10:15:23	1.956
3C 204	08:37:44.9, +65:13:35	1.112
3C 205	08:39:06.4, +57:54:17	1.534
3C 208	08:53:08.8, +13:52:55	1.110
3C 212	08:58:41.5, +14:09:44	1.048
3C 245	10:42:44.6, +12:03:31	1.029
3C 268.4	12:09:13.6, +43:39:21	1.398
3C 270.1	12:20:33.9, +33:43:12	1.532
3C 287	13:30:37.7, +25:09:11	1.055
3C 318	15:20:5.40, +20:16:06	1.574
3C 325	15:49:58.4, +62:41:22	1.135
4C 16.49	17:34:42.6, +16:00:31	1.880
3C 432	21:22:46.2, +17:04:38	1.785
3C 454.0	22:51:34.7, +18:48:40	1.757

their host galaxies. For the SED analysis, we have compiled the X-ray to radio SED by combining archival data from Chandra, XMM-Newton, Sloan Digital Sky Survey (SDSS), UKIRT, Two Micron All Sky Survey (2MASS), Spitzer, Wide-field Infrared Survey Explorer (WISE), Herschel, and multifrequency radio observations. The photometry is aperture corrected. The X-ray data used in this analysis are from Wilkes et al. (2013), and the optical and UV data are gathered from the references available on NASA/IPAC Extragalactic Database. The NIR to FIR photometry used here is drawn from Podigachoski et al. (2015). Table 2 indicates the submillimeter fluxes recently obtained from The Submillimeter Array (SMA) or Atacama Large Millimeter/submillimeter Array (ALMA) for our analysis. Tables A1–A3 in the Appendix present the radio observations (with their references) used in our analysis.

We assembled the final SEDs from these data sets by selecting the highest-quality photometry. Photometric measurements that showed significant deviations from the majority in that wavelength range were removed. We excluded photometry with signal-to-noise ratio (S/N) < 3 at any wavelengths except at FIR and submillimeter wavelengths, where the upper limits are the only constraints available. Finally, we note that the visible-UV photometry is not contaminated by emission lines. We fitted a power-law continuum in IRAF (Tody 1986) to regions of the SDSS or Hubble Space Telescope (HST) spectrum that were uncontaminated by emission lines using the continuum windows of Kuraszewicz et al. (2002). The power law was then binned into 10–15 continuum bins and included in our SEDs. The spectra and photometry are both dereddened for Galactic absorption (see Section 3.3 for more details).

3. SED Components and the Fitting Routine

One of the most important advantages of this study relative to previous work is that it accounts for emission over 10 decades in frequency, from radio to X-ray. Because both AGNs and host galaxies contribute throughout the electromagnetic spectrum, it is critical to disentangle the contributions from each as a function of wavelength in order to quantify the

Table 2
Recent Submillimeter Data Obtained with the SMA or ALMA

Name	ν (GHz)	Flux Density (mJy)	Telescope
3C 212 ^a	98	106 ± 5	ALMA
3C 212 ^a	233	41 ± 2	ALMA
3C 245 ^b	224	84 ± 1	SMA
3C 270.1 ^c	235	13.5 ± 0.3	SMA
3C 318 ^d	315	2.3 ± 0.6	ALMA
3C 454.0 ^d	315	10.6 ± 1.4	ALMA

Notes.

^a PI: Meyer; Proposal ID: 2019.1.01709.S.

^b PI: Ashby; Proposal ID: 2019B-S034.

^c PI: Ashby; Proposal ID: 2019A-S031.

^d PI: Podigachoski; Proposal ID: 2015.1.00754.S.

contributions of the various physical mechanisms to the overall energy budget. In this section, we first describe the components used in our SED model (ARXSED) to account for the AGN emission, and then describe those used to model the emission from the host galaxy. Additionally, we describe the methods used to correct for the obscuration from the torus, the host galaxy, and the Milky Way absorption along the line of sight.

3.1. The AGN Components in ARXSED

Here we treat the models accounting for the AGN emission as arising from three components: an accretion disk, an obscuring torus, and radio lobes.

3.1.1. The Accretion Disk Component

For the accretion disk, we use the QSOSED model developed by Kubota & Done (2018). The primary variable parameters in this model are presented in Table 3. Adopting a geometrically thin disk, Kubota & Done (2018) assumed that the emission from the accretion disk originates in three distinct regions: an inner region extending from the innermost stable circular orbit (R_{ISCO}) to R_{hot} , an intermediate region extending from R_{hot} to R_{warm} , and an outer region from R_{warm} to R_{out} . Accretion disk radii R_{warm} and R_{hot} , respectively, define the boundaries of warm and hot Comptonization regions, and R_{out} is the outer edge of the accretion disk (for more details, see the Appendix of Kubota & Done 2018). In this framework, the inner region has a temperature of ~ 100 keV and includes the hot corona with no underlying disk (i.e., a truncated disk). The plasma in the inner region emits the X-ray power-law component. In the intermediate region, warm Comptonization occurs, and the soft X-ray excess is produced. The electron temperature in the intermediate region is ~ 0.2 keV, and the optical depth is ~ 10 –25 (e.g., Czerny et al. 2003; Gierliński & Done 2004; Petrucci et al. 2013; Middei et al. 2018). The nature of the warm Comptonization is not completely understood (e.g., Done et al. 2012). This may result from a failed, UV-driven wind arising in the outer disk region that falls back down into the disk (Laor & Davis 2014). The outer disk region, which has a temperature of a several thousand kelvin, is the standard optically thick accretion disk dominated by blackbody emission.

The QSOSED model fixes the accretion disk parameters to typical AGN values of $kT_{e,\text{hot}} = 100$ keV, $kT_{e,\text{warm}} = 0.2$ keV, $\Gamma_{\text{warm}} = 2.5$, $R_{\text{warm}} = 2R_{\text{hot}}$, and $R_{\text{out}} = R_{\text{self gravity}}$ which define, respectively, the electron temperatures for the hot and warm

Table 3
Parameters Used in Constructing the Accretion Disk Templates with the QSOSED Model

Parameter	Initial Estimate	Range of Variation	Steps	Acceptable Range
$\log(M_{\text{BH}})$	M_0 (C IV or Mg II)	$[\log(M_0) - 1, \log(M_0) + 1]$	0.2 dex	[7,10]
$\log(\lambda_{\text{Edd}})$...	$[-1.65, 0.39]$	0.2 dex	$[-1.65, 0.39]$
spin (1)	...	$[0.75^a, 0.998]$	0.02	$[0, 0.998]$
inclination angle (θ_D)	$\theta_{\text{T(torus)}}$	$[\theta_{\text{T}} - 12, \theta_{\text{T}} + 12]$	θ_{T} dependent	$[0, 90]$

Note. 1) Templates with lower spin values (0–0.75) were examined for a subsample of our sources. However, none of those templates resulted in a better accretion disk fit.

Comptonization components, the spectral index of the warm Comptonization component, and the radii of the regions. The spectral index of the hot Comptonization component, Γ_{hot} , is calculated via Equation (6) of Kubota & Done (2018). The QSOSED model also includes reprocessed radiation, which is the fraction of the hot Comptonization component’s emission that heats both the warm Comptonized material and the cool outer disk.

The primary variables in the QSOSED model are the SMBH mass M_{BH} , the mass accretion rate (which is traced with the Eddington ratio defined in Equation (1)), the inclination angle, and the dimensionless spin parameter $a \equiv Jc/GM_{\text{BH}}^2$, where J is the angular momentum of the BH. Figure 1 illustrates the effect that variation of each parameter has on the shape of the visible, UV, and X-ray SEDs. Overall, the effects of varying these parameters on the geometry of the accretion disk and on its SED are intertwined. For example, increasing BH mass while holding mass accretion rate and other parameters constant results in a more luminous but cooler accretion disk. Increasing the Eddington ratio results in a more luminous and hotter accretion disk. Increasing the spin moves the R_{ISCO} closer to the SMBH and the peak toward higher energies and increases the radiative efficiency. As spin increases toward maximally rotating, its impact on the SED shape becomes more noticeable, but lower spins have no significant impact on the peak and shape of the accretion disk SED. In all cases, a face-on observer sees more of the UV bump than an edge-on observer.

To fit the visible-to-X-ray SED of each quasar, we construct a set of QSOSED templates in XSPEC¹⁰ covering a range for each parameter and using any available information to set the initial parameter values (e.g., BH mass). To construct the templates for each quasar, we varied each parameter with a fixed step within their acceptable ranges in QSOSED. Table 3 summarizes the initial estimates, range of variation, steps used in our procedure, and the acceptable range for each parameter in the model.

Out of 20 sources in our sample, six (3C 9/191/205/270.1/432/454.0) have a broad C IV $\lambda 1548$ line and six (3C 14/181/186/204/245/268.4) have a broad Mg II $\lambda 2800$ line (SDSS archive, private communication; Barthel et al. 1990), which we used to estimate the BH masses. For the remaining quasars, we used the median BH mass of these 12 sources as the initial mass estimate. BH mass measurements based on the high ionization C IV line have larger errors than those estimated from the Mg II or Balmer lines (e.g., Sulentic et al. 2002; Baskin & Laor 2005; Shen 2013). However, we used this mass

only as the initial estimate and allowed M_{BH} to vary within ± 1 dex of this value (in steps of 0.2 dex.) Because there is no prior information on $\log m$, we allowed it to vary over the entire acceptable range (in steps of 0.2 dex). Radio-loud quasars are expected to have high spin values (see Reynolds 2019, and references therein) so we used a limited range from 0.75¹¹ to 0.998 (in steps of 0.02). For the accretion disk’s inclination angle, we used the best-fit value from the torus model (Section 3.1.2) and then varied the inclination angle within $\pm 12^\circ$. However, rather than using a fixed step size, we determined seven values within $\pm 12^\circ$ of the initial estimate empirically.¹² Overall, we constructed $\sim 11,000$ templates to fit the visible-X-ray SED of each quasar.

3.1.2. The Torus Component

We adopted the two-phase AGN torus model developed by Siebenmorgen et al. (2015). The model assumes the dust around the AGN can be described as a clumpy medium, a homogeneous disk, or a combination of both. Siebenmorgen et al. (2015) defined the inner radius (R_{in}) of the dusty structure by the sublimation temperature of the dust grains. The outer radius of the structure is $R_{\text{out}} = R_{\text{in}} \times 170$, which is chosen to be large enough to have a negligible impact on the observed features in the FIR SED. The density of the dust decreases with radius. The dust grains are fluffy mixtures of silicate and amorphous carbon grains (Krügel & Siebenmorgen 1994) instead of the interstellar medium (ISM) dust grains (e.g., Siebenmorgen et al. 2014). These fluffy grains are more efficient absorbers and have higher submillimeter emissivities than the diffuse ISM grains (for more details, see Section 2.6 of Siebenmorgen et al. 2015).

Table 4 lists the primary variable parameters and their possible values in the model. These parameters are the inner radius of the dusty structure (R_{in}), the optical depth of the homogeneous disk midplane (τ_D), the optical depth of the clumps (τ_C), the volume filling factor (V_C), and the torus inclination angle (θ_{T}). Varying these parameters within their acceptable range makes a library with 3600 templates. These templates are built for an AGN of luminosity $10^{11} L_{\odot}$. Since the SEDs are scale-invariant, the inner radius scales (see Table 6) with the square root of the actual luminosity of the primary source, i.e., the accretion disk, (e.g., Suganuma et al. 2006; Kishimoto et al. 2011).

¹¹ We tested lower spin values (0–0.75) for a subsample of our sources. However, none of those templates resulted in a better accretion disk fit.

¹² We note that the viewing angle from the torus was used as an initial estimate to build the accretion disk templates. However, studies support the connection between the torus and the accretion disk inclination angles (among other parameters, including the Eddington ratio; Calderone et al. 2012; Campitiello et al. 2021).

¹⁰ XSPEC is an interactive program used to fit spectral models to data from visible to gamma-rays. For more information, see <https://heasarc.gsfc.nasa.gov/xanadu/xspec/>.

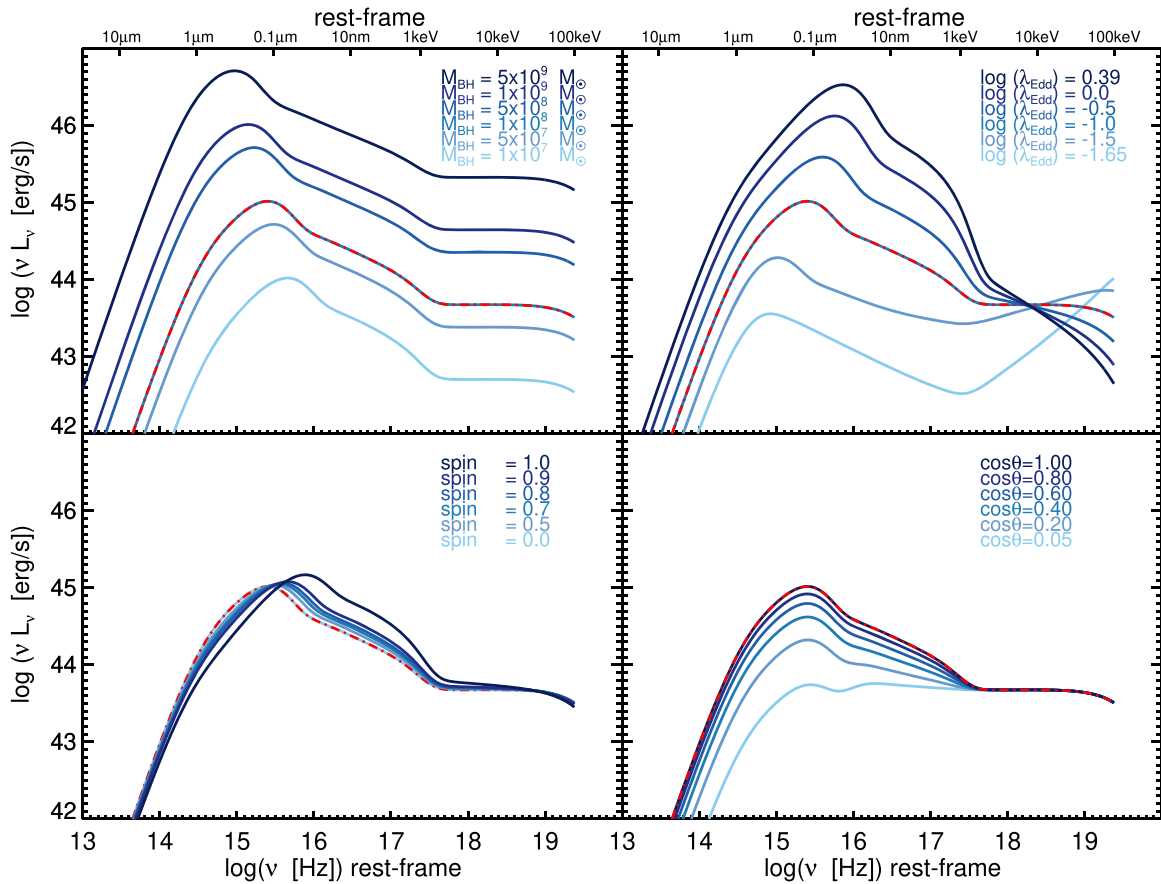


Figure 1. QSOSED model parameters (Kubota & Done 2018) as a function of rest-frame frequency and wavelength. Clockwise from top left, the parameters varied are BH mass, Eddington ratio, spin, and the inclination angle. In each panel, the red dotted–dashed line indicates the reference model in which $M_{\text{BH}} = 10^8 M_{\odot}$, $\log(\lambda_{\text{Edd}}) = -1.0$, $\text{spin} = 0$, and $\cos\theta = 1$. Additional curves illustrate the impacts of varying the indicated parameter while holding all other parameters constant.

Table 4

Free Parameters and Their Possible Values in the Siebenmorgen et al. (2015) Torus Library

Parameter	Acceptable Values
Inner radius ^a (R_{in})	300, 514, 772, 1000, 1545 ($\times 10^{15}$ cm)
Cloud volume filling factor (V_C)	1.5, 7.7, 38.5, 77.7 (%)
Cloud optical depth (τ_C)	0, 4.5, 13.5, 45
Disk optical depth (τ_D)	0, 30, 100, 300, 1000
Torus inclination angle (θ_T)	19, 33, 43, 52, 60, 67, 73, 80, 86 ($^\circ$)

Note.

^a The inner radius is the dust sublimation radius and scales with the total AGN luminosity as $R_{\text{in}} \propto \sqrt{L_{\text{AGN}}}$. The values listed here are for an AGN of a luminosity of $10^{11} L_{\odot}$.

Figure 2 illustrates the impact of varying each parameter on the NIR–FIR SED. As R_{in} increases, the torus moves farther from the central engine; therefore, the emission of hotter dust grains becomes less pronounced, and the peak of the torus SED moves to longer wavelengths. The impacts of variation of the filling factor and optical depth of the clumps are intertwined. An increase in V_C and/or τ_C (when the other parameters are unchanged) results in more absorption at shorter wavelengths (see the variation of a silicate emission feature to an absorption feature at $9.7 \mu\text{m}$), and a shift of the peak of the SED to longer wavelengths due to the higher density of the clouds closer to the central engine. An increase in the opacity of the homogeneous disk (τ_D) results in more scattering from the

disk surface, which acts similarly to adding more dust grains with a range of temperatures (for a face-on observer). Therefore the emissions from short and long wavelengths both increase. However, this will not be the same for an edge-on observer (see Figures 4 and 5 in Siebenmorgen et al. 2015). As the observer’s inclination angle changes from face-on toward edge-on, the observer sees less of the emission from the inner parts of the torus (short wavelengths) and, rather than a silicate emission feature, sees an absorption feature. Our fitting procedure, in general, does not have any prior information to limit the torus parameters, but in a few cases, the observed silicate feature helped to constrain the torus model (see Section 4.1).

As noted in the introduction, the MIR emission from the torus comes from the absorbed and reprocessed UV and visible photons radiated by the accretion disk. Therefore, the SED shape of the primary source of emission might influence the reprocessed MIR radiation. The primary source of radiation in Siebenmorgen et al. (2015) is the Rowan-Robinson (1995) model, which describes the visible-UV continua of quasars with a broken power-law function. Instead, we use the Kubota & Done (2018) accretion disk model (see Section 3.1.1). We examined the impact of various accretion disk models (including a simple blackbody and a few others; Kubota & Done 2018) on the torus SED and found that the SED shape longward of $1 \mu\text{m}$ (rest frame) is independent of the chosen accretion disk template at wavelengths shorter than $1 \mu\text{m}$; i.e., the torus essentially acts as a calorimeter.

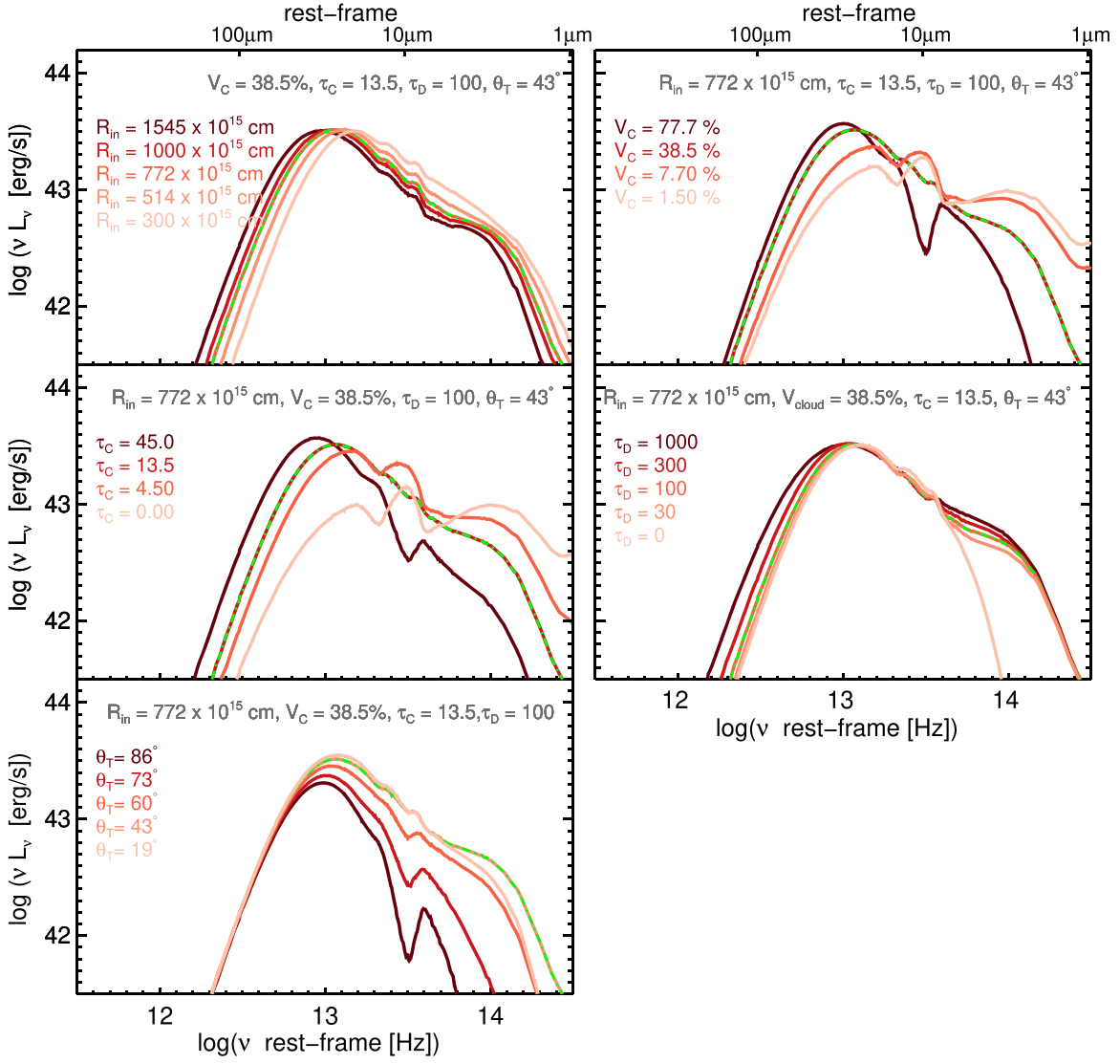


Figure 2. An illustration of the impacts of varying one parameter of the torus SED model while holding all other parameters constant. The parameters include the inner radius of the torus (R_{in}), the volume filling factor of the clumps and their optical depth (V_C and τ_C), the optical depth of the homogeneous disk (τ_D), and the inclination angle. The green dotted–dashed line shows the reference model in which $R_{\text{in}} = 772 \times 10^{15}$ cm, $V_C = 38.5\%$, $\tau_C = 13.5\%$, and $\tau_D = 100$, and $\theta_T = 43^\circ$.

3.1.3. The Radio Component

Table 5 lists the salient radio properties of our sample sources, including their usual classification as a compact steep spectrum (CSS; see references in Wilkes et al. 2013) and their radio-core dominance parameter (Orr & Browne 1982), which is the ratio of 5 GHz radio-core to extended radio-lobe emission

$$R_{\text{CD}} = L_{(\text{core}, 5 \text{ GHz})} / L_{(\text{lobe}, 5 \text{ GHz})}. \quad (2)$$

We also list projected radio jet lengths measured lobe-to-lobe at 178 MHz (taken from the compilation of C. Willott) in Table 5¹³ as well as the radio jet’s inclination angle, within $\pm 10^\circ$ (estimated from the radio-core fraction; Marin & Antonucci 2016). The de-projected radio jet lengths (and their range) are also listed.

To fit the radio emission from the quasars in our sample, we started by considering a relativistic electron population with a

power-law energy distribution in a magnetic field of strength B :

$$N(E) \propto E^{-p}. \quad (3)$$

Synchrotron emission is generated by these relativistic electrons spiraling around magnetic field lines. While some of this emission is absorbed by the electrons in optically thick regions (synchrotron self-absorption), radio photons from optically thin regions reach the observer. We can formulate synchrotron emission transitioning from an optically thick, self-absorbed region to an optically thin region with the radiative transfer equation (for more details, see Section 4.4–4.7 in Ghisellini 2013):

$$I(\nu) = \frac{\epsilon_\nu}{\kappa_\nu} (1 - e^{-\tau_\nu}); \quad \tau_\nu \equiv R\kappa_\nu \quad (4)$$

in which τ_ν is the spectral optical depth, R is the size of the emitting region, ϵ_ν is the emissivity, and κ_ν is the specific

¹³ <http://astroherzberg.org/people/chris-willott/research/3crr/>

Table 5
Radio Properties of the Quasars in Our Sample

Name	Type ^a	R_{CD} ^b	Projected Jets Length ^c (kpc)	Inclination Angle ^d (°)	De-projected Jets Length ^e (kpc)	Range of De-projected Jets Length ^f (kpc)
3C 009	...	0.009	85	52±10	151	[135, 178]
3C 014	...	0.018	213	42±10	308	[261, 389]
3C 043	CSS	<0.060	26	>26	<49	...
3C 181	...	0.009	59	49±10	65	[57, 77]
3C 186	CSS	0.042	16	42±10	20	[17, 25]
3C 190	CSS	0.098	25	27±10	124	[94, 194]
3C 191	...	0.102	34	31±10	81	[64, 116]
3C 204	...	0.087	296	34±10	543	[437, 748]
3C 205	...	0.0309	154	38±10	251	[208, 330]
3C 208	...	0.105	107	32±10	172	[136, 243]
3C 212	...	0.204	73	20±10	216	[147, 425]
3C 245	...	1.950	40	4 ⁺¹⁰ ₋₄	1067	[307, -]
3C 268.4	...	0.091	85	27±10	205	[155, 319]
3C 270.1	...	0.282	103	16±10	374	[235, 987]
3C 287	CSS	... ^g	8
3C 318	CSS	<0.138	9	58±10	8	[7, 9]
3C 325	...	0.003	124
4C 16.49	...	0.052	145	39±10	216	[180, 281]
3C 432	...	0.025	111	46±10	155	[134, 190]
3C 454.0	CSS	<0.339	10	>14	<46	...

Notes.^a Compact steep spectrum (CSS; see references in Wilkes et al. 2013).^b Radio-core dominance (R_{CD} , see Equation (2)).^c Projected radio sizes, measured lobe-to-lobe from high-resolution images at 5 GHz.^d Jet inclination angle (Marin & Antonucci 2016).^e De-projected radio sizes, measured lobe-to-lobe at 178 MHz.^f The range of the de-projected sizes estimated from the range of the inclination angles in Column 4.^g We did not find the R_{CD} estimate for 3C 287 in the literature, so we adopted the average values of the other CSS quasars as an upper limit.

absorption coefficient. These can be approximated by

$$\epsilon_\nu \propto B^{(p+1)/2} \nu^{-(p-1)/2} \quad (5)$$

$$\kappa_\nu \propto B^{(p+2)/2} \nu^{-(p+4)/2}. \quad (6)$$

When $\tau_\nu \gg 1$ (in a self-absorbed regime), the second component in the radiative transfer equation becomes negligible, and Equation (4) can be simplified to:

$$I(\nu) = I_0(\nu) \propto B^{-1/2} \nu^{5/2} \quad (7)$$

which is independent of p (see Section 4.5 in Ghisellini 2013). Setting ν_t to be the frequency at which the transition from optically thick to thin occurs, then

$$\tau_{\nu_t} \equiv R\kappa_{\nu_t} = 1, \quad (8)$$

and using Equation (6), we then obtain

$$\nu_t \propto [RB^{(p+2)/2}]^{2/(p+4)}. \quad (9)$$

Therefore

$$\tau_\nu \equiv R\kappa_\nu = \left(\frac{\nu_t}{\nu}\right)^{(p+4)/2} = \left(\frac{\nu_t}{\nu}\right)^{(p-1)/2+5/2}. \quad (10)$$

Now if $\alpha_2 = -(p-1)/2$ is the spectral index in the optically thin region, and $\alpha_1 = 5/2$ is the spectral index in the optically

thick region, we can rewrite Equation (4) as

$$I(\nu) \propto \left(\frac{\nu}{\nu_t}\right)^{\alpha_1} \left[1 - \exp\left(-\left(\frac{\nu_t}{\nu}\right)^{\alpha_1-\alpha_2}\right)\right]. \quad (11)$$

As the electron population ages, it loses its energy, and eventually, the synchrotron radiation terminates at a cutoff frequency. This can be approximated by adding an exponential factor (Polletta et al. 2000):

$$L_\nu \propto \left(\frac{\nu}{\nu_t}\right)^{\alpha_1} \left[1 - \exp\left(-\left(\frac{\nu_t}{\nu}\right)^{\alpha_1-\alpha_2}\right)\right] e^{-\frac{\nu}{\nu_{\text{cutoff}}}}. \quad (12)$$

Equation (12) describes radiation from both optically thick and thin regions, which terminates at high energies due to energy loss. This equation is based on many assumptions, including the charged particle being an electron, the electron population's energy having a power-law distribution, the source is homogeneous, and therefore $\alpha_1 = 2.5$. In order to describe the radio emission from the quasars in our sample, we used the general form presented in Equation (12) and modified it based on different conditions.

Model 1–Single Power Law with an Exponential Cutoff: In an AGN in which the radio emission is dominated by radiation from the optically thin lobes, a power law can successfully describe the radio emission (Polletta et al. 2000):

$$L_\nu \propto \left(\frac{\nu}{\nu_{\text{cutoff}}}\right)^{\alpha_2} e^{-\frac{\nu}{\nu_{\text{cutoff}}}}. \quad (13)$$

Model 2–Double Power Law with an Exponential Cutoff: The added presence of compact structures such as radio cores

and hot spots may cause the spectral shape to deviate from a single power law. In this model, we assumed a double power law similar to Equation (12). However, α_1 was treated as a free parameter, not fixed at 2.5 (because we do not expect a single, homogeneous component), and ν_t is the transition frequency from α_1 - to α_2 -dominated regions.

Model 3–Parabola with a Cutoff: Relaxing the homogeneous assumption, our third model assumes a parabolic function that approximates a superposition of multiple power-law components, some optically thick and some thin (Cleary et al. 2007):

$$\log L_\nu \propto -\beta(\log \nu - \log \nu_t)^2 + \log(e^{-\frac{\nu}{\nu_{\text{cutoff}}}}). \quad (14)$$

β in this equation indicates the curvature of the parabola.

Overall, Equation (12) or Equation (14) can successfully describe the emission from a source with a mix of optically thick and thin regions (e.g., a lobe-dominated quasar with bright hot spots or a moderately bright core).

Model 4–Parabola with a Cutoff and Double Power Law with an Exponential Cutoff: In quasars with bright cores, the superposed self-absorbed components may generate spectral shapes not amenable to fitting with simple models. Our fourth model is a combination of Equations (12) and (14), where Equation (12) is solely used to describe the radio-core emission, and Equation (14) describes radiation from the lobes and hot spots. In this case, the core and lobe components each have their own cutoff frequency.

We fit the above four models to the observed radio photometry using the MPFIT nonlinear least-square fitting function in IDL (Markwardt 2009). The spectral slopes α_1 and α_2 in each model as well as β and ν_t are free parameters, and the cutoff frequency was limited to $10^{10} < \nu_{\text{cutoff}} < 10^{14}$ Hz.

3.2. The Host Galaxy Component

We used the MAGPHYS SED code (da Cunha et al. 2008, 2015) to account for the emission from the host galaxy. MAGPHYS is capable of accounting simultaneously for different levels of star formation activity, stellar populations, dust obscuration, and SFHs for galaxies at different redshifts. We note that MAGPHYS does not include any AGN component, and to fit the emission from an AGN, we used the models described in Section 3.1.

MAGPHYS is built upon the energy balance technique, which links the UV and visible emission from the young stellar population to the IR emission from dust. In other words, starlight is the only source of dust heating, and the energy absorbed by dust is equal to the re-radiated energy. The stellar emission from UV to NIR wavelengths is modeled with the Bruzual & Charlot (2003) spectral population synthesis model (assuming a Chabrier 2003 IMF) attenuated by dust following Charlot & Fall (2000). The model assumes the young stars form in dense clouds (i.e., giant molecular clouds); when younger, their emission is attenuated by the dust in their birth cloud and the ambient ISM, but as they age, the birth clouds disappear on a timescale of 10^7 yr, and the stellar emission is then absorbed only by the diffuse ISM (Charlot & Fall 2000). MAGPHYS considers four dust components, each including grains with a different size and temperature: polycyclic aromatic hydrocarbon grains, hot grains with temperatures in the range 130–250 K, grains in thermal equilibrium with the temperature of 30–60 K, and cold dust grains with adjustable

equilibrium temperature in the range 15–25 K. The stellar birth clouds contain the first three dust components, and cold dust only exists in the ambient ISM (see da Cunha et al. 2008 for more details).

Although the original da Cunha et al. (2008) MAGPHYS code covers a broad wavelength range from 912 Å to 1 mm, here we use the updated da Cunha et al. (2015) version, which includes the galaxy contribution at radio wavelengths (for more details, see Section 3.2 in da Cunha et al. 2015). In addition to broader wavelength coverage, the more recent version includes a continuous delayed exponential SFH:

$$\Psi(t) \propto \gamma^2 t \exp(-\gamma t) \quad (15)$$

in which t is the time since the onset of star formation, and $\gamma = 1/\tau_{\text{SF}}$ is the inverse of the star formation timescale (see Lee et al. 2010; da Cunha et al. 2015). da Cunha et al. (2015) also included absorption by the IGM, which can strongly impact the UV emission in high-redshift galaxies such as the ones treated here.

Although the da Cunha et al. (2015) model includes galaxy emission at radio wavelengths, the radio emission (both thermal and nonthermal components) in galaxies is 4–5 orders of magnitude lower than that in radio-loud AGNs. Therefore, AGNs are the dominant sources of radio emission in the present analysis.

3.3. Dereddening and Absorption Corrections

In order to obtain the intrinsic SED of the AGNs in our sample, it is necessary to correct the photometry for the absorption occurring at various wavelengths. In brief, these corrections include correcting the X-ray observations for host galaxy and Milky Way absorption, correcting the UV–NIR photometry for Milky Way absorption, and correcting the visible-UV radiation from the accretion disk for dusty torus absorption.

X-ray photons are absorbed by the gas in their host galaxies (i.e., intrinsic) and along the line of sight in the Milky Way. We adopted the best estimates of the X-ray luminosity from Wilkes et al. (2013), i.e., corrected for both intrinsic and Galactic absorption. Additionally, we corrected the UV–NIR (0.91–13.0 μm) photometry for absorption by the Milky Way using the attenuation law of $\tau_\lambda \propto \lambda^{-0.7}$ from Charlot & Fall (2000).

To estimate the extinction of the accretion disk emission from the obscuring structure in the torus, we used the method of Siebenmorgen et al. (2015; see also Krügel 2009). According to this method, the effective optical depth for any templates (with any combination of dust clouds and homogeneous disk) can be obtained via comparison to the flux of that template in the absence of dust (see Section 2.7 in Siebenmorgen et al. 2015):

$$\tau_{\text{eff}} = -\ln \frac{f_{(\text{best-fit-template})}}{f_{(\text{no-dust-template})}}. \quad (16)$$

Thus, we first determined the template that best fits the NIR–FIR data corresponding to the AGN emission (not the host galaxy; see Section 3.4 for more details) and then applied Equation (16) to estimate the effective optical depth. The visible–UV photometry (corresponding to the accretion disk emission) was then corrected by a factor of $e^{\tau_{\text{eff}}}$ for the absorption in the torus. Depending on the best fit, τ_{eff} may be a

negative or positive number indicating scattering or absorption by the dust structure. An edge-on observer is not able to see the scattered light from the torus and is mainly affected by absorption, i.e., a positive τ_{eff} , while a face-on observer sees the scattered light from the torus and is not affected by absorption, i.e., a negative τ_{eff} (see Siebenmorgen et al. 2015).

3.4. Fitting Methodology

In this Section, we describe our fitting methodology and the steps in which the various attenuation and absorption corrections from Section 3.3 are applied.

In radio-loud quasars, AGN emission dominates that of the host galaxy over most of the SED. Therefore, we allowed the contribution of the AGN to the photometry at submillimeter to UV wavelengths to vary from 95%–65% (in bins of 5%) of the total. At radio and X-ray wavelengths, the host galaxy contribution is orders of magnitude smaller than the AGN. At IR to UV wavelengths, torus and accretion disk emission, which dominate the SED, were allowed to vary independently from one another. The variation of the AGN components contributions results in an iterative process:

Step 1: The fitting procedure starts by determining the torus templates that best fit the photometry associated with the AGN at IR wavelengths. The torus templates of Siebenmorgen et al. are normalized to an AGN of luminosity $10^{11} L_{\odot}$ (Section 3.1.2). Therefore, we integrate the luminosity of each AGN within the range of 2–45 μm (rest frame) and normalize the torus templates according to this integrated luminosity for each source. We then determine the best-fit torus model using χ^2 minimization.

Step 2: We corrected the visible–UV photometry associated with the accretion disk for the torus reddening, implementing the correction factor obtained from Equation (16). To do this, we assumed the line of sight to the accretion disk is the same as that for the torus. We then fitted the accretion disk templates, built for this sample (see Section 3.1.1), to the visible-UV and X-ray photometry and identified the best-fit accretion disk template via χ^2 minimization.

Step 3: We fitted the radio photometry with the four models described in Section 3.1.3 and determined the best fit using χ^2 minimization. We normalized the radio models to the 5 GHz photometry. In the fourth radio model, we used the 5 GHz core flux density to normalize the core component and the remaining flux density to normalize the parabola component. We inspected the radio images in several bands (178 MHz, 5 GHz, 8 GHz, and 15 GHz, if available) to check the consistency of any preference for multicomponent models with different spectral indices with the presence of bright hot spots and/or core emission.

Step 4: We subtracted the best-fit AGN component (radio, torus, and accretion disk) from the total observed photometry and fit this residual with MAGPHYS to account for the host galaxy contribution. To include the upper limits in MAGPHYS, we followed the prescription of da Cunha et al. (2015) in which the flux densities are set to zero, and the upper limit values are set as the uncertainty.

Step 5: We found the total fit by combining the AGN and the host galaxy components.

Step 6: We repeated Steps 1–5 above for all combinations of the torus and the accretion disk normalizations (95%–65% in bins of 5%). We also examined the cases with 100% or <65% contributions from the AGN components. However, none of

those resulted in a better fit than the one presented. In particular, the torus component cannot replicate the emission at FIR to submillimeter wavelengths, and an underlying host galaxy component is required. We identified the best fit as the one that not only results in low χ^2 values for the total fit but individual components.

We note that after identifying the best-fit torus model via χ^2 minimization, we examined the impact of varying the torus parameters on the visible-UV SED and the total fit. This is particularly important for the so-called red quasars in our sample. These are reddened Type 1 AGNs in which the visible-UV SED lacks the big blue bump and have red MIR colors (e.g., Benn et al. 1998; Cutri et al. 2001; Lacy et al. 2004; Georgakakis et al. 2009; Kim & Im 2018). In our fitting routine, we assume that the reddening is due to the torus obscuration and examined the dependence of the shape of the intrinsic visible-UV SED on the torus parameters to obtain a reasonable UV bump in the red quasars. In this procedure, the obscuration from the host galaxy at visible-UV bands is assumed to be negligible. For the red quasars in our sample (3C 14/190/212/325), the galactic hydrogen column densities $N_{\text{H,gal}}$ are 15–375 times less than the torus N_{H} (Wilkes et al. 2013), which indicates the absorption from the host galaxy is much less than the torus.¹⁴ We describe the best-fit model to each of these sources in Section 4; however, understanding the nature of red quasars is beyond the scope of this paper.

4. Radio to X-Ray SED Analysis of the 3CRR Quasars at $1 < z \lesssim 2$

In this section, we apply ARXSED to the 3CRR quasar sample at $1 < z \lesssim 2$, and describe the results. We first describe the details of the best-fit AGN model for individual sources and then summarize the commonalities among sources.

4.1. Fitting Results for Individual Sources

The parameters for the best-fit accretion disk and torus and radio models are given in Tables 6 and 7. Figure 3 shows the full suite of photometry together with the best-fit models. The gray data points are the absorption-corrected broadband photometry, and the black plus signs in visible-UV bands indicate the photometric points before the torus obscuration correction. The components in these plots are radio components from the core, jets, and lobes (light blue), IR emission from the torus that contributes at rest-frame wavelengths longward 1 μm (dark red), the accretion disk component that accounts for the thermal optical to X-ray emission (green), the host galaxy component obtained from the MAGPHYS SED fitting code (magenta), and the total fit (orange). The dark-blue star indicates the core contribution to the 5 GHz photometry estimated from the R_{CD} presented in Table 5. The X-ray photometry was extracted within a $2''.2$ aperture centered on the X-ray source position, sized to match the full Chandra point-spread function, and so is dominated by the nuclear X-ray emission (Wilkes et al. 2013). The black line (and the bow tie for sources with higher X-ray counts) at the X-ray point indicates the power-law fit to the absorption-corrected data. The SED fits are presented in 3CRR number order below.

3C 9 has de-projected jets of ~ 151 kpc and a core contribution of less than 1% at 5 GHz. The radio emission in

¹⁴ 3C 68.1, excluded from our sample (see Section 2), is a red quasar that required additional correction from the host galaxy.

Table 6
Parameters of the Best-fit Torus and Accretion Disk Model

Name	$R_{\text{in}}(\text{pc})^{\text{a}}$	$V_{\text{C}}(\%)^{\text{b}}$	$\tau_{\text{C}}^{\text{c}}$	$\tau_{\text{D}}^{\text{d}}$	$\theta_{\text{T}}(^{\circ})^{\text{e}}$	$\theta_{\text{AD}}(^{\circ})^{\text{f,i}}$	$M_{\text{BH}}(\times 10^9 M_{\odot})^{\text{i}}$	$\log(\lambda_{\text{Edd}})^{\text{g,i}}$	$\text{Spin}^{\text{h,i}}$
3C 009	3.74	1.5	0	1000	52	48 ± 6	3.8 ± 1.2	-0.4 ± 0.2	0.98 ± 0.04
3C 014	4.53	77.7	0	100	67	57 ± 7	9.6 ± 1.4	-0.4 ± 0.4	0.92 ± 0.02
3C 043	1.80	1.5	45	100	60	70 ± 2	2.1 ± 0.7	-1.0 ± 0.2	$0.99 -0.01$
3C 181	2.85	1.5	45	300	52	59 ± 8	1.7 ± 0.7	-0.6 ± 0.1	0.92 ± 0.08
3C 186	2.75	1.5	4.5	300	52	62 ± 7	1.5 ± 0.5	-0.6 ± 0.5	$0.99 -0.02$
3C 190	5.95	1.5	45	300	60	63 ± 4	6.0 ± 1.3	-1.0 ± 0.1	$0.99 -0.03$
3C 191	6.53	1.5	45	300	43	43 ± 5	1.8 ± 0.0	-0.6 ± 0.2	0.92 ± 0.02
3C 204	2.59	77.7	0	300	52	55 ± 6	2.9 ± 0.0	-1.0 ± 0.2	0.98 ± 0.03
3C 205	5.79	7.7	4.5	300	52	55 ± 6	9.8 ± 0.0	-0.8 ± 0.5	0.92 ± 0.01
3C 208	2.09	1.5	4.5	300	52	48 ± 6	1.5 ± 1.2	-0.4 ± 0.5	$0.99 -0.01$
3C 212	1.71	7.7	4.5	300	60	53 ± 2	6.0 ± 0.0	-1.2 ± 0.1	0.96 ± 0.00
3C 245	7.94	1.5	0	30	19	26 ± 7	1.1 ± 0.0	-0.6 ± 0.2	0.98 ± 0.02
3C 268.4	2.29	1.5	45	1000	52	52 ± 7	6.2 ± 2.3	-1.0 ± 0.2	$0.99 -0.04$
3C 270.1	2.55	1.5	45	1000	52	50 ± 5	4.6 ± 0.9	-1.0 ± 0.9	0.98 ± 0.02
3C 287	1.16	38.5	0	1000	19	26 ± 0	1.5 ± 0.8	-1.2 ± 0.1	0.99 ± 0.00
3C 318	1.30	1.5	45	1000	33	38 ± 9	2.4 ± 0.8	-1.6 ± 0.2	0.98 ± 0.02
3C 325	0.75	1.5	13.5	300	60	49 ± 2	3.8 ± 0.0	-1.4 ± 0.0	0.88 ± 0.02
4C 16.49	1.19	7.7	0	1000	43	55 ± 0	2.1 ± 0.7	-1.4 ± 0.0	0.94 ± 0.02
3C 432	3.07	38.5	0	1000	33	46 ± 9	4.7 ± 1.4	-1.2 ± 0.2	$0.99 -0.01$
3C 454.0	4.53	1.5	4.5	1000	43	51 ± 9	0.8 ± 0.0	0.0 ± 0.1	$0.99 -0.04$

Notes.^a The inner radius of the best-fit torus ($R_{\text{in}} \propto \sqrt{L_{\text{AGN}}/10^{11}L_{\odot}}$).^b The volume filling factor of the clumps.^c The optical depth of the individual clumps.^d The optical depth of the homogeneous disk midplane.^e The inclination angle of the torus.^f The inclination angle of the accretion disk.^g The Eddington ratio ($\lambda_{\text{Edd}} \propto L_{\text{bol}}/L_{\text{Edd}}$).^h The dimensionless spin parameter $a \equiv Jc/GM_{\text{BH}}^2$ where J is the angular momentum of the SMBH.ⁱ The reported uncertainties in the accretion disk parameters are standard deviations derived from the 5% of the fits with the lowest χ^2 values.

Table 7
Parameters of the Best-fit Radio Model

ID	Best Radio Model ^d	ν_{r}	$\nu_{\text{r,jet}}$	α_1	α_2	β	ν_{cutoff}	$\nu_{\text{cutoff,jet}}$
3C 009	2	5.5e+07	...	-0.09	-1.04	...	5.7e+11	...
3C 014	2	3.8e+10	...	-0.91	-2.15	...	1.0e+13	...
3C 043	1	-0.75	...	1.5e+12	...
3C 181	1	-0.94	...	8.1e+11	...
3C 186	3	5562.3	10.28	8.3e+12	...
3C 190	2	4.7e+07	...	1.98	-0.92	...	4.9e+12	...
3C 191	1	-0.99	...	3.0e+12	...
3C 204	2	1.1e+07	...	1.37	-1.10	...	1.0e+12	...
3C 205	2	5.1e+07	...	1.34	-0.98	...	2.1e+11	...
3C 208	2	1.9e+08	...	-0.14	-1.16	...	1.0e+12	...
3C 212	4	1000.1	1.5e+10	2.20	-0.52	7.46	5.0e+11	7.5e+11
3C 245	4	3814.4	7.9e+08	2.50	-0.35	9.41	8.1e+12	5.1e+11
3C 268.4	2	6.9e+09	...	-0.71	-1.17	...	3.0e+12	...
3C 270.1	2	5.6e+07	...	1.35	-0.90	...	1.0e+12	...
3C 287	2	1.8e+09	...	-0.13	-0.79	...	1.3e+12	...
3C 318	2	4.3e+08	...	-0.07	-1.01	...	2.0e+11	...
3C 325	2	1.7e+09	...	-0.50	-1.12	...	2.2e+11	...
4C 16.49	2	4.2e+08	...	-0.40	-1.17	...	1.0e+11	...
3C 432	2	1.1e+09	...	-0.64	-1.19	...	2.8e+11	...
3C 454.0	3	600.4	5.92	1.8e+12	...

Note.^a 1: single power law with an exponential cutoff, 2: single power law with an exponential cutoff, 3: parabola with a cutoff, 4: parabola with a cutoff and double power law with an exponential cutoff.

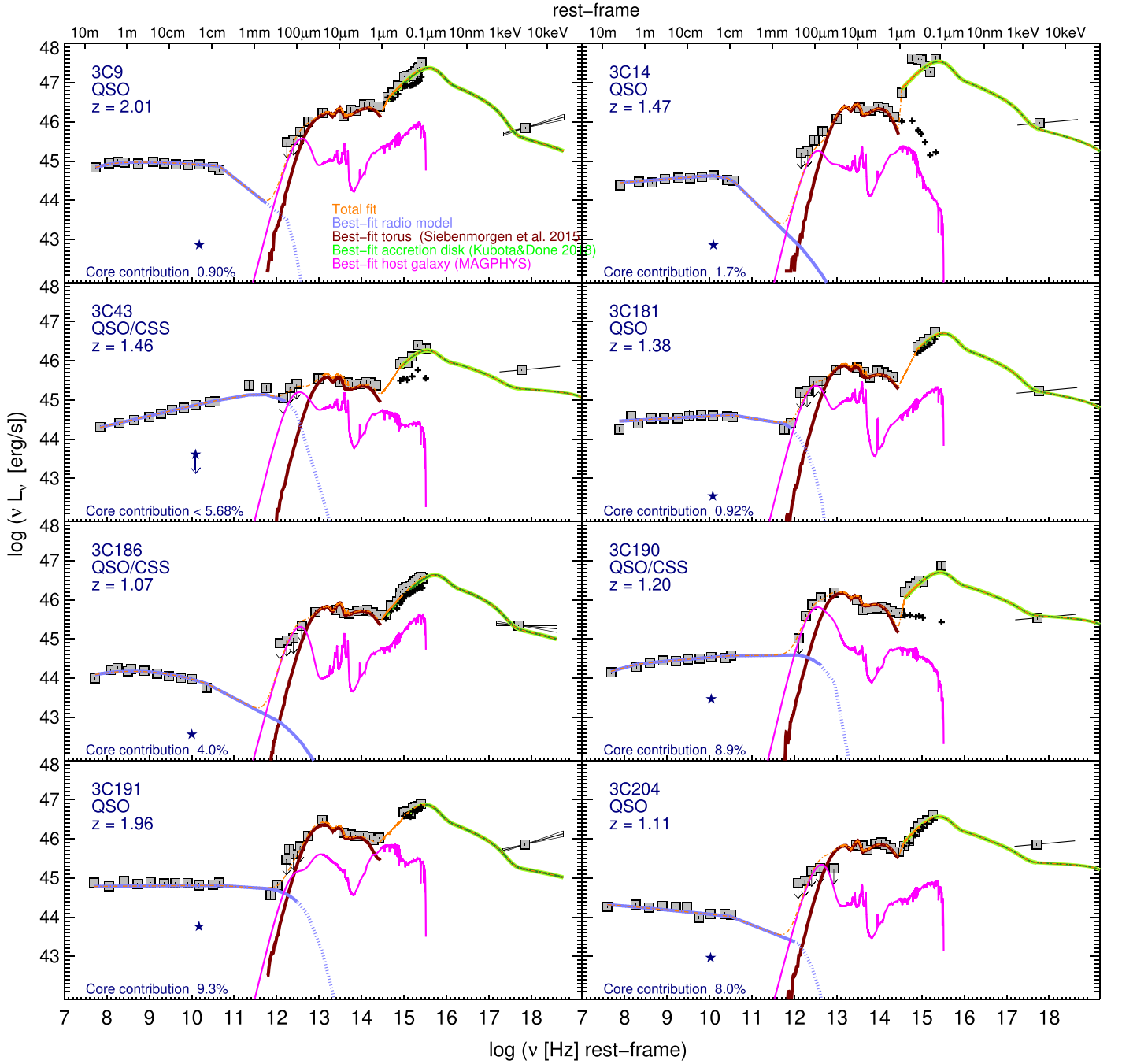
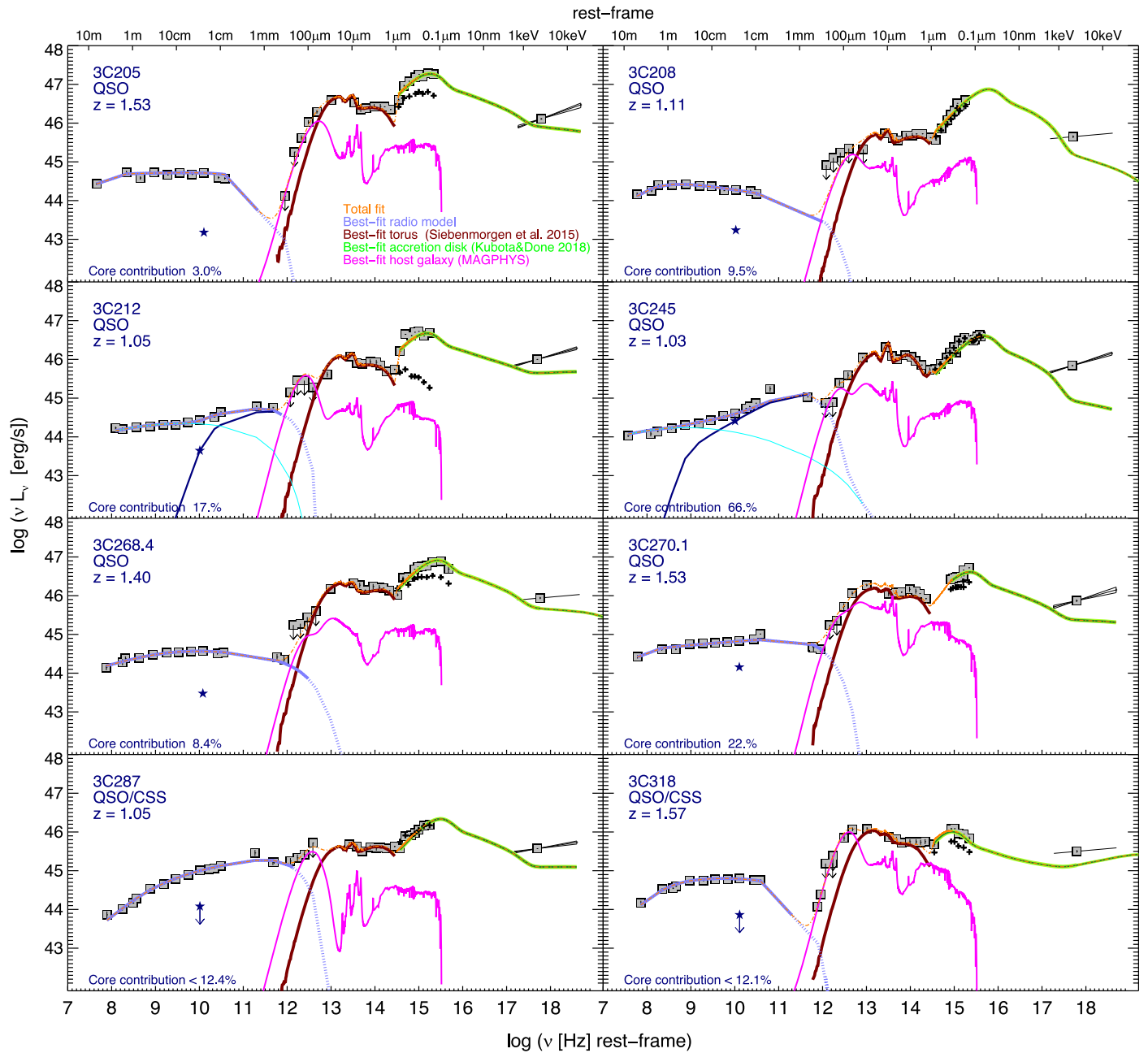


Figure 3. (a) The full suite of photometry with the best-fit models of the 3CRR quasars at $1 < z \lesssim 2$. The gray data points show the absorption-corrected broadband photometry, and the black plus signs in visible-UV bands are the photometric points before the torus obscuration correction. The lines represent radio emission from the core, jets, hot spots, and lobes (light blue), IR emission from the torus (dark red), thermal visible to X-ray emission from the accretion disk (green), the underlying host galaxy emission (magenta), and the total fit (orange). The radio emission truncates at the cutoff frequency (where the dotted line begins). The dark-blue star indicates the core contribution to the 5 GHz photometry estimated from R_{CD} . The black line (and the bow tie for sources with higher X-ray counts) at X-ray indicates the power-law fit to the absorption-corrected data. (b) In the case of 3C 212/245, the cyan parabola component indicates the emission from the extended structures, while the dark-blue component indicates the emission from the core.

this source is best described as a broken power law (with an exponential cutoff at 570 GHz; see Table 7), which is consistent with the presence of multiple features (i.e., jet, counter-jet, bright hot spots based on 4.9 GHz Very Large Array (VLA) data; Bridle et al. 1994).

The emission from the torus is best described with a combination of clumps with negligible opacity and a

homogeneous disk with the highest allowed optical depth (see Table 4). The filling factor and optical depth of the clumps indicate that there is not much obscuration from the dust clouds along the line of sight. Therefore, the correction of the visible-UV emission from the torus obscuration is negligible. For this object, the inclination angle from the best-fit torus model is 52° while from the best-fit accretion disk template, it is 63° . As



noted in Section 3.1.1 the accretion disk templates are built within the range of $\pm 12^\circ$ from the inclination angle of the best-fit torus model.

The accretion disk template lies below the X-ray data, suggesting the presence of a nonthermal X-ray component. Chandra observations (Fabian et al. 2003) found extended X-ray emission on both sides of the nucleus of 3C 9 coincident with the radio structure and suggested it is probably due to nonthermal inverse Compton emission from the interaction of the relativistic electrons with the cosmic microwave background. While the X-ray data used in our analysis is nuclear, there might still be some contribution from the extended X-ray emission, which might result in the discrepancy between the accretion disk fit and X-ray data.

3C 14 is a red quasar (Smith & Spinrad 1980) with less than 2% core contribution at 5 GHz and extended radio jets of 308 kpc. The radio emission is best described with a broken power law with an exponential cutoff at FIR wavelengths, consistent with the multiple radio structures present in MERLIN 18 cm data (Akujor et al. 1994). SED fitting shows that the nonthermal emission at submillimeter/FIR wavelengths is negligible.

The emission from the torus is best described with a combination of clumps with negligible opacity and a homogeneous disk with moderate optical depth. However, this, combined with the inclination angle of 67° results in substantial (more than 1 order of magnitude) obscuration of the visible-UV emission. The visible-UV SED before obscuration correction

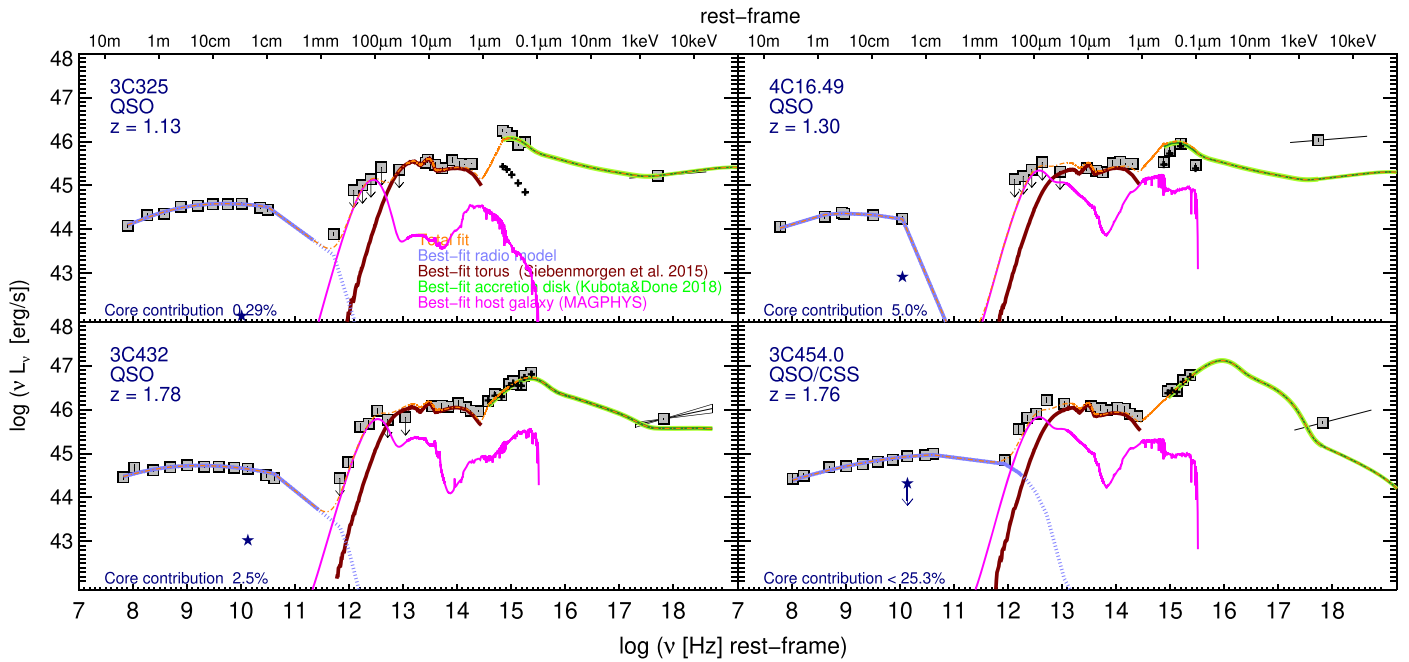


Figure 3. (Continued.)

(shown in black plus signs) is consistent with its classification as a red quasar. As noted in Section 3.4, we examine the impact of the variation of the torus parameters on the intrinsic visible-UV SED in our fitting procedure to make sure the best-fit torus model results in a reasonable accretion disk SED. Our SED fitting indicates that the classification of 3C 14 as a red quasar is related to the inclination angle rather than a dustier torus. Using the length of the radio jets as a proxy of AGN maturity (e.g., Podigachoski et al. 2015) indicates that 3C 14 is a mature quasar. Therefore it is unlikely for this source to be in an evolutionary phase in which it turns from an obscured quasar into an unobscured one. To investigate the impact of the host galaxy obscuration on the visible-UV SED of this source, we will include this source when analyzing the NLRG in our sample and examine whether the correction from the host galaxy can improve the SED fit at visible-UV bands.

The X-ray spectrum is well fit by the accretion disk model, implying no significant contribution from the radio structures at X-rays.

3C 43 is a CSS quasar with jets of <49 kpc and a core contribution of $<6\%$ at 5 GHz (Akujor et al. 1991; Ludke et al. 1998). The radio emission is best described with a single power law with an exponential cutoff at FIR wavelengths. Akujor et al. (1991) indicated that this source has a misaligned and asymmetric structure with a sharp bent jet suggesting that the presence of the bent structure in this source could be due to the interaction of the jets with the ISM.

The best-fit torus model is a combination of clumps with a small volume filling factor and a homogeneous disk with low opacity that result in a small amount of obscuration of the visible-UV emission.

As illustrated in Figure 3 the millimeter and submillimeter data are dominated by nonthermal radiation from the radio structures. The submillimeter-excess could be attributed to the interaction of the jets with the gas along their paths. Further investigation with ALMA is required to understand the nature of submillimeter radiation. However, the best-fit accretion disk

template also confirms the presence of a significant possibly jet-triggered X-ray component. Podigachoski et al. (2015) reported the presence of a bright nearby object dominating at the PACS 160 μm band. The potential nonthermal emission from the radio structures and the contaminating nearby object add uncertainty to the estimated host galaxy star formation rate (SFR).

3C 181 has radio jets of 65 kpc with $<1\%$ core contribution at 5 GHz (Mantovani et al. 1992). The radio emission is best described with a single power law with an exponential cutoff at 814 GHz. Willott et al. (2002) investigated the 850 μm band SCUBA observation of this source and predicted no non-thermal component contributing to this wavelength.

The best-fit torus is a combination of clumps with a small filling factor and a homogeneous disk with moderate opacity, which results in little correction of the visible-UV emission.

Comparing the best-fit accretion disk with the X-ray data does not indicate the presence of an underlying X-ray component triggered by the radio structures.

3C 186 is a very well studied CSS (O’Dea 1998) with radio jets of 20 kpc and 4% core contribution at 5 GHz (Spencer et al. 1991; Ludke et al. 1998). Radio emission is best described with a parabola (a combination of multiple power laws). MERLIN observation at 1.6 MHz indicates a one-sided jet and two bent lobes at 60° and 90° with respect to the source axis, creating an S-shaped source (Spencer et al. 1991; Ludke et al. 1998). The curvature in the lobes is presumably due to the sufficiently dense ISM that affects the expansion of the radio structure.

The best-fit torus is a combination of clumps with a small filling factor and a homogeneous disk with moderate opacity, which results in no significant correction of the visible-UV emission.

The Chandra and HST observations indicate that 3C 186 lives in an overdense region, which is most likely a cluster of galaxies (Siemiginowska et al. 2010; Hilbert et al. 2016). The HST images indicate a blob of star formation activity $2''$

(corresponding to ~ 16 kpc at $z \sim 1$) away from the central engine, perpendicular to the direction of the jets (see Figure 10 in Hilbert et al. 2016).¹⁵ This blob could be either from the star formation activity of other members of the cluster or from the host galaxy itself. In the latter case, given that the jets' direction is perpendicular to the blob, the star formation activity is not jet-related. Comparing the best-fit accretion disk with the X-ray data does not indicate the presence of an underlying jet-triggered X-ray component.

3C 190 is a red quasar (Ishwara-Chandra et al. 2003) CSS and has de-projected radio jet lengths of 124 kpc, and less than 1% core contribution at 5 GHz. The radio images (Spencer et al. 1991; Ludke et al. 1998) indicate multiple features that require a double power law in our fitting procedure (see Table 7). As shown in Figure 3, the radio emission cutoff occurs at FIR wavelengths. While this suggests that the nonthermal emission may contribute significantly at submillimeter wavelengths (hence, SFR estimates based on submillimeter data should be treated carefully), submillimeter observations are required for constraining the radio fit.

The emission from the torus is best described with a combination of clumps and a homogeneous disk with maximum acceptable opacity in the torus library (see Table 4). This, combined with a small filling factor and 43° inclination angle, results in moderate obscuration of the visible-UV emission of the accretion disk. While quasar spectra, in general, show silicate emission features, the rest-frame 9–16 μm spectra of 3C 190 indicate the presence of silicate absorption (Leipski et al. 2010). In our fitting procedure, we examined the torus templates with silicate absorption; however, none of those results in a better fit than that shown in Figure 3.

Comparing the best-fit accretion disk with the X-ray data does not indicate the presence of an underlying X-ray component triggered by radio structures.

3C 191 was classified as a CSS in some earlier studies (Akujor & Garrington 1995; Willott et al. 2002); however, using the classification of Podigachoski et al. (2015) and radio jets of 81 kpc we do not classify this object as a CSS. 3C 191 has $\sim 9\%$ core contribution at the 5 GHz, and its radio emission is best described as a single power law with a cutoff at FIR wavelengths (see Table 7). Therefore, as illustrated in Figure 3, the submillimeter data and likely FIR have a significant nonthermal contribution.

The emission from the torus is best described with a combination of clumps with a low volume filling factor and a homogeneous disk with moderate opacity and an inclination angle of 43° , which implies no significant obscuration of the accretion disk emission. The low level of obscuration is consistent with the optical spectral slope, α_{opt} , of 0.7 (Barthel et al. 1990), which is a typical value of radio quasars with little obscuration (see also Brotherton et al. 2001; Willott et al. 2002).

3C 191 spectra indicate the presence of a strong absorbing system (rest-frame equivalent width of 6.1 \AA) associated with C IV absorption line (Anderson et al. 1987) ~ 30 kpc from the nucleus (Hamann et al. 2001). Studies find that quasars with strong associated absorption lines are in the early stage of their development, and smaller/younger radio structures are more common to have associated absorption lines (e.g., Becker et al. 2000, 2001; Willott et al. 2002). However, as discussed in

detail in Barthel et al. (2017), the absorption feature in 3C 191 is possibly connected to starburst-driven superwinds (see also Hamann et al. 2001).

In most of our sources (see Figure 3), the torus component dominates the blue side of the FIR bands; interestingly, in 3C 191, it dominates over the host galaxy emission at all of the MIR-FIR bands. The Herschel upper limits in the FIR allow for the possibility of a weak, FIR, cool dust contribution below the submillimeter wave band where the synchrotron component dominates. 3C 191 was classified as a hyperluminous quasar with $L_{\text{FIR}} > 1.2 \times 10^{13} L_{\odot}$ (Willott et al. 2002). However, we find the torus to be the dominant source of IR emission rather than the host galaxy.

Finally, we note that the best-fit accretion disk model indicates the presence of a nonthermal X-ray component possibly associated by radio structures.

3C 204 has an extended jet of ~ 543 kpc and $\sim 8\%$ core contribution in the 5 GHz band. The quasar radio SED is well fitted with a broken power law (see Table 7). The VLA 4.9 GHz images show multiple features, including a bright radio core, hot spots, and a one-sided jet that deflects toward the end (Bridle et al. 1994). There is some evidence of [O II] emission perpendicular to the jet axis (Bremer et al. 1992; Bridle et al. 1994) at ~ 90 kpc toward the north and ~ 45 kpc toward the south.

The emission from the torus is best described with a combination of clouds with negligible optical depth and a homogeneous disk with moderate opacity. This, combined with an inclination angle of 52° results in no significant obscuration of accretion disk at visible-UV.

Comparing the best-fit accretion disk model with the X-ray data suggests the presence of additional, nonthermal X-ray emission possibly triggered by radio jets.

3C 205 has extended radio structures of ~ 251 kpc with a core contribution of 3% in the 5 GHz band. The radio emission is best described as a broken power law (see Table 7), which is consistent with the presence of the multiple radio structures (Lonsdale & Barthel 1984, 1986).

The emission from the torus is best described with a combination of clumps with small opacity and a homogeneous disk with moderate opacity, which result in a small amount of obscuration of the accretion disk radiation. 3C 205 spectra indicate the presence of a strong absorbing system (rest-frame equivalent width of $\text{jhc}3.21 \text{\AA}$) associated with C IV absorption line (Anderson et al. 1987).

The best-fit accretion disk model predicts the presence of little nonthermal radiation at the X-ray band triggered by radio structures.

3C 208 has a radio jet of ~ 172 kpc with $\sim 10\%$ core contribution at 5 GHz. The radio emission is best fitted with a broken power law that is consistent with the presence of multiple radio features, including a bright core and the hot spots (Bridle et al. 1994). 3C 208 has a one-sided jet that is straight for most of its length but deflects toward the end (Bridle et al. 1994).

The emission from the torus is best described with a combination of clumps with a small optical depth and a homogeneous disk with moderate opacity, which result in no significant obscuration at visible-UV wavelengths. The available HST images (F606W and F140W bands) do not indicate any evidence of nearby merging sources (Hilbert et al. 2016).

¹⁵ We note that the HST data are not included in our SED analysis.

The X-ray spectrum fitted by the accretion disk model implies some contribution from the radio structures.

3C 212 is a red quasar (Aldcroft et al. 2003) with radio jets of ~ 216 kpc and $\sim 17\%$ core contribution at 5 GHz. MERLIN observations at 6 cm and 15 cm (Akujor et al. 1991) indicate multiple features including a bright core that is best fitted with the fourth model in our fitting procedure (see Section 3.1.3 and Table 7). In this case, the cyan component indicates the emission from the extended radio structures/hot spots, and the dark-blue component illustrates the emission from the core. We note that each component is truncated at its own cutoff frequency. To constrain the radio fit, we used recent ALMA observations (see Table 2), which are dominated by the nonthermal radiation from the radio structure (Figure 3).

Consistent with its classification as a red quasar, our torus model indicates a combination of clumps and a homogeneous disk with moderate optical depth. These components result in moderate obscuration of the accretion disk emission. This target also has X-ray and UV absorbers (Aldcroft et al. 2003).

The X-ray spectrum fitted by the accretion disk model implies the presence of an X-ray component possibly triggered by the radio structures.

3C 245 is a moderately beamed quasar (with a jet oriented at $<20^\circ$ to the line of sight; Foley & Barthel 1990; Marin & Antonucci 2016) with ~ 1067 kpc jets and $\sim 66\%$ core contribution at 5 GHz, which is significantly higher than other sources in our sample (see Table 5). The radio emission is best described as a parabola (shown in cyan) with an additional core component (shown in dark blue). To constrain the radio contribution to the FIR, we recently obtained the SMA data (see Table 2), which is dominated by the nonthermal radiation from the radio structure (Figure 3). The extreme variability expected in blazars may not be seen in 3C 245 since our recent SMA observation is consistent with older radio data (Geldzahler & Witzel 1981).

Consistent with its classification, the best-fit torus indicates a combination of clumps with negligible opacity and a homogeneous disk with small opacity. This combination results in no significant obscuration from the clouds and the homogeneous dusty disk. The torus inclination angle (19° ; see Table 6) and the accretion disk inclination angle (26°) are consistent with the radio-determined inclination angle (Foley & Barthel 1990; Marin & Antonucci 2016).

The best-fit accretion disk model also indicates the presence of significant nonthermal X-ray emission possibly triggered by the radio structures. We note that since 3C 245 has nearly a face-on inclination angle and significant underlying nonthermal radiation at radio/millimeter and X-ray wavelengths, the nonthermal continuum may contribute significantly to the IR-visible-UV bands as well. Given the significant nonthermal emission and quasars' dominance at visible-UV bands, it is unlikely to have a reliable estimate of the host galaxy properties from our SED fits.

3C 268.4 has jets of 205 kpc and $\sim 8\%$ core contribution at 5 GHz. The radio images (Lonsdale & Barthel 1986; Liu et al. 1992) indicate multiple features, including a bright core and double hot spots. The radio emission is best fitted with a double power-law model with a cutoff at FIR wavelengths (see Table 7), resulting in significant nonthermal contribution at submillimeter wavelengths (Willott et al. 2002).

The emission from the torus is best described with a combination of clumps and a homogeneous disk with the

highest acceptable opacity in the torus library (see Table 4). However, this, combined with a small filling factor and inclination angle of 52° , results in little obscuration of the accretion disk emission. Similar to 3C 191, 3C 268.4 is also classified as a hyperluminous quasar with $L_{\text{FIR}} > 2 \times 10^{13} L_\odot$ (Willott et al. 2002). Similar to 3C 191, we find more contribution from the torus than the host galaxy in the 160 and $350 \mu\text{m}$ bands. We also note that similar to 3C 191, the spectra of 3C 268.4 show strong CIV associated absorption (Anderson et al. 1987).

3C 268.4 was reported as a lensed quasar with a foreground cluster at $z \sim 0.35$ (Sanitt 1976). We did not correct the SED for the magnification by the foreground cluster. Recent HST observations indicate the presence of a bright star-forming clump $2''.5$ from the center and an additional oblong source with both optical and radio emission $0''.8$ from the center (see Figure 10 in Hilbert et al. 2016). Since the IR emission from these structures cannot be resolved from AGN emission with the current data, the hyperluminous quasar classification should be treated with caution (see 3C 318 below).

The X-ray spectrum fitted by the accretion disk model implies no significant contribution from the radio structures.

3C 270.1 has a jet of ~ 374 kpc and a relatively high core contribution (22%) at 5 GHz. Multifrequency radio images of 3C 270.1 indicate the presence of a strong core and hot spots (Liu et al. 1992) and a one-sided jet (Hilbert et al. 2016). The radio emission is best fitted with a double power law with a cutoff at FIR wavelengths resulting in significant nonthermal contribution at millimeter wavelengths.

The emission from the torus is best described with a combination of clumps with a small filling factor and a homogeneous disk with the highest acceptable opacity in the torus library. This, combined with a 52° inclination angle, results in little reddening of the accretion disk emission.

3C 270.1 spectra indicate the presence of a strong absorption complex (rest-frame equivalent width $>6.17 \text{ \AA}$) associated with CIV absorption line (Anderson et al. 1987).

The best-fit accretion disk model indicates the presence of significant emission at the X-ray wave band possibly triggered by radio structures. Chandra observations find extended X-ray emission that is copatial with the radio lobe and peaks at the position of the hot spots (Wilkes 2012). The extended X-ray emission is not included in the X-ray data used for this SED analysis.

3C 287 is a CSS with projected radio jets of ~ 8 kpc. Because the jet inclination angle for this object is unknown, we were unable to estimate its de-projected jet length. Also, we were unable to find the R_{CD} value for this object; therefore, we adopted the average value of the CSS quasars in our sample (Section 3.1.3), which resulted in $\sim 10\%$ core contribution. The radio emission is modeled as a double power law with a cutoff at submillimeter/FIR wavelengths (see Table 7), resulting in significant nonthermal contribution at millimeter to submillimeter wavelengths. The VLBI and MERLIN observations indicate the presence of multiple radio structures, including a curving jet (Fanti et al. 1989).

The emission from the torus is best described with a combination of clumps with a negligible optical depth and a homogeneous disk with the highest acceptable opacity in the torus library (see Table 4). This combination with the inclination angle of 19° (26° from the accretion disk model) results in no significant obscuration of the visible-UV radiation

from the accretion disk. While the extreme variability is expected in moderately beamed quasars, it may not be seen in CSS and GPS sources such as 3C 287, since they are young (e.g., Salvesen et al. 2009).

The X-ray spectrum fitted by the accretion disk model implies a significant contribution associated with the radio structures. The X-ray data obtained with XMM-Newton and Chandra (Salvesen et al. 2009; Wilkes et al. 2013) find a soft X-ray spectrum ($\Gamma = 1.8$) that can be fitted with a simple power law.

Similar to 3C 245, 3C 278 is viewed almost face-on and has significant underlying nonthermal radiation at radio/submillimeter and X-ray wavelengths. The nonthermal continuum may contribute to other wavelengths. We also note that the HST images indicate a few nearby sources ($\sim 5''$; Hilbert et al. 2016), and the IR emission may be contaminated by one/more of these sources. Altogether, these make the host galaxy properties estimated from our SED fits uncertain.

3C 318 is a CSS with jets of ~ 8 kpc and core contribution $< 12\%$ at 5 GHz. The 18 cm MERLIN and VLBI observations (Spencer et al. 1991) show a two-sided jet, which fades before reaching the lobes. The emission from the radio structure is best described with a double power law with a cutoff at 200 GHz. In addition to the 1.2 mm MAMBO data, we used recent ALMA observations (see Table 2 and Barthel & Versteeg 2019) to constrain the radio model. Barthel & Versteeg (2019) used the 2 cm VLA image to subtract the nonthermal emission from the ALMA image at 1 mm and estimated that $\sim 11\%$ of the total flux at 1 mm has a nonthermal origin. We use this estimate to constrain the radio model in our fitting procedure. However, with this prior estimate, the cutoff in our fitting procedure happens at ~ 200 GHz; consequently, we estimate no nonthermal contribution at 1 mm. Therefore, there could be $\lesssim 10\%$ nonthermal contribution at submillimeter wavelengths (also see Haas et al. 2006).

The torus emission is best described with a combination of clumps and a homogeneous disk, both with high opacity. However, due to the small filling factor of the clumps and the 33° inclination angle, these components do not result in a significant obscuration of the accretion disk emission.

The best-fit accretion disk indicates the presence of an additional X-ray component possibly triggered by radio structures. We note that with only a few data points at the optical, UV, and X-ray range, the physical parameters driven from the accretion disk model (see Table 6) should be treated with caution.

We note that 3C 318 is classified as a hyperluminous IR quasar with $L_{\text{FIR}} > 10^{13} L_\odot$ in some earlier studies (Willott et al. 2002, 2007). Recently, Podigachoski et al. (2016b) reported that most of the fluxes measured in earlier studies originate in a pair of bright interacting galaxies at $z \sim 0.35$. To robustly estimate the AGN and host galaxy properties, we used the fluxes from Table 1 in Podigachoski et al. (2016b). After subtracting the contamination of the nearby source from the photometry, 3C 318 has an SFR of $\sim 320 M_\odot \text{ yr}^{-1}$, a factor of 5 lower than the Willott et al. (2007) estimation.

3C 325 was originally classified as a radio galaxy and later was reclassified as a red quasar (Grimes et al. 2005) based on optical spectroscopic data. This quasar has a projected radio jet of 124 kpc and less than 1% core contribution at 5 GHz. Because the jet inclination angle for this object is unknown, we were unable to estimate its de-projected jet length. The VLA

images show multiple features, including bright hot spots and asymmetrically placed lobes (Fernini et al. 1997). The radio data are best fitted with a double power law, which turns down before reaching the submillimeter wavelengths.

Consistent with its X-ray spectral analysis ($N_{\text{H}} \sim 6.2 \times 10^{22} \text{ cm}^{-2}$; Wilkes et al. 2013), the emission from the torus is best described with a combination of clumps and a homogeneous disk with moderate opacity. This combination results in moderate obscuration of the accretion disk emission. Considering the lack of data in $1\text{--}3 \mu\text{m}$ (observed-frame), the best-fit accretion disk is determined with the data points at shorter wavelengths; therefore, the accretion disk parameters are not well constrained.

The best-fit accretion disk does not imply the presence of nonthermal X-ray emission. The X-ray analysis indicates a moderately hard X-ray spectrum with the hardness ratio (H-S/H+S, where H and S are the net count rates in the 2–8 keV and 0.5–2 keV X-ray bands) of +0.05, which is harder than all of the other quasars in our sample (Wilkes et al. 2013).

4C 16.49 extends over 216 kpc with $\sim 5\%$ core contribution at 5 GHz. The radio images obtained with VLA at 2 and 6 cm show a strong radio core, jet, and a small counter-jet (Lonsdale et al. 1993). The radio emission is best described with a double power law (see Table 7). Our model does not predict any nonthermal contribution from the radio structures at shorter wavelengths; however, due to the small number of reliable data points and lack of millimeter and submillimeter data, we should be cautious in the interpretation of the results.

The best-fit torus model combines clumps with negligible opacity and a homogeneous disk with the highest acceptable opacity in the torus library (see Table 4). This combination results in no significant obscuration of visible-UV emission from the accretion disk.

The best-fit accretion disk template also confirms the presence of a significant X-ray component possibly triggered by radio structures. However, unlike other sources in our sample, 4C 16.49 does not have SDSS or other recent reliable data at visible-UV wavelengths and is only limited to old SuperCOSMOS observations. Given the limited number of visible-UV photometric measurements, the accretion disk may not be well constrained, and the X-ray component from the radio structures may not be significant.

3C 432 extends over ~ 155 kpc and has a core contribution of $\sim 3\%$ at 5 GHz. The VLA images indicate multiple structures, including radio lobes, bright hot spots, and a one-sided jet (Bridle et al. 1994). The emission from these radio structures is best described with a double power law (Table 7).

The torus emission is best fitted with a combination of clumps with negligible opacity, and a homogeneous disk with high opacity that are viewed at 33° inclination angle and result in no significant obscuration of the accretion disk emission. The HST F606W and F140W images show extended narrow-line regions (within $8''$) along the direction of the radio lobes (Hilbert et al. 2016) with several faint sources within this radius, which could potentially contaminate the quasar SED.

The X-ray spectrum fitted by the accretion disk implies no contribution from the radio structures to the X-ray emission.

3C 454.0 is a CSS with de-projected jets of < 46 kpc and $< 25\%$ core contribution at 5 GHz. The radio images show various features, including the core and hot spots (Spencer et al. 1991; Ludke et al. 1998). The radio emission is best described with a parabola having a cutoff at FIR wavelengths. To

constrain the radio model, we added recent ALMA data to our analysis (see Table 2 and Barthel & Versteeg 2019). We used the nonthermal emission estimated in Barthel & Versteeg (2019) as prior information to constrain the radio model in our fitting procedure. Similar to Barthel & Versteeg (2019), we estimate $\sim 82\%$ nonthermal emission at 1 mm.

The torus emission is best fitted with a combination of clumps with small opacity and a homogeneous disk with the maximum acceptable τ_D in the torus library (see Table 4). This combination at an inclination angle of 43° results in no significant obscuration of the accretion disk emission.

The X-ray spectrum fitted by the accretion disk implies contribution from the radio structures at X-ray wavelengths.

4.2. Commonalities among Sources

1. Out of the 20 quasars in our sample, 11 (3C 43/181/190/191/212/245/268.4/270.1/287/454.0) have $>90\%$ non-thermal contamination at 1.25 mm (see Section 5.5 for more details). While the millimeter to submillimeter emission in some of these sources is dominated by the core (3C 212/245), in others it can be dominated by the extended structures and hot spots.
2. In 13 sources (3C 9/43/191/204/208/212/245/268.4/270.1/287/318/454.0 and 4C 16.49), there are discrepancies between the best-fit accretion disk and the X-ray data. Different factors may contribute to these discrepancies. X-ray emission associated with radio structures may be present, especially for sources with high R_{CD} (e.g., 3C 245/270.1). This may confirm a jet-related contribution to the X-ray emission in radio-loud quasars and may contradict findings (see Zhu et al. 2020) that attribute the X-ray brightness of the radio-loud quasar (relative to the radio-quiet population) to the corona rather than the jet. Potential contamination from the extended X-ray emission in our X-ray luminosity estimation and underestimation of the X-ray emission in radio-loud AGNs in the Kubota & Done (2018) accretion disk model are also possible factors contributing to the discrepancies.
3. In sources with small inclination angles (3C 245/287), the significant underlying nonthermal radiation at radio to submillimeter and X-ray wavelengths may contribute at IR, visible, and UV bands as well. Therefore, the torus and the host galaxy properties derived from SED fitting are uncertain.
4. The HST data (F606W and F140W bands; Hilbert et al. 2016) of some of our sources (3C 268.4/287 and maybe 3C 432) indicate the presence of a few nearby objects, which may contaminate the photometry. In these cases, the physical properties derived from SED fitting are poorly unconstrained.
5. Four quasars in our sample 3C 191/205/268.4/270.1, with de-projected radio jets of 81, 251, 205, and 374 kpc have associated C IV absorption complexes (Anderson et al. 1987) with rest-frame equivalent widths of 6.12 Å, 3.21 Å, >1.87 Å, and >6.17 Å, respectively. While some studies (e.g., Becker et al. 2000, 2001; Willott et al. 2002) suggest that associated absorption is more common in sources with smaller/younger radio structures, there does not appear to be such a relationship in our sample.
6. Our SED modeling is limited by the available photometry (see Section 5.1). In sources with few reliable visible-UV

data points (3C 14/318/325 and 4C 16.49), the accretion disk parameters may be poorly constrained.

7. Extinction in the red quasars (3C 14/190/212/325) is primarily due to a highly inclined torus rather than the dust extinction in the host galaxy.

5. Discussion

In this study, we present a state-of-the-art AGN radio-to-X-ray SED model (ARXSED) that decomposes radio-loud quasars into their AGN and host galaxy components by fitting their photometry over 10 decades in frequency space. With ARXSED, we investigate the properties of a sample of 20 3CRR quasars at $1 < z \lesssim 2$. Below we first discuss the uniqueness and limitations of our technique, as well as the average properties of the AGNs in our sample. We then present the median SED of the radio-loud quasars obtained with our fitting technique. Finally, we compare the details of our model, the median SED, and the properties of our quasars with the literature.

5.1. Uniqueness, Limitations, and Biases of ARXSED

An advantage of this study compared to previous works (e.g., Kuraszekiewicz et al. 2003; Mullaney et al. 2011; Podigachoski et al. 2015, 2016b) is the wavelength coverage. ARXSED treats photometry extending from radio to X-ray wavelengths. Specifically, ARXSED models the radio emission (Section 3.1.3), the torus (Section 3.1.2), and the accretion disk (Section 3.1.1) as well as the host galaxy (Section 3.2). Thus, it simultaneously accounts for radiation from different structures surrounding the SMBHs. While ARXSED considers a component that accounts for the host galaxy emission from radio to UV wavelengths, some studies rely on scaling relations such as $M_{BH} - \sigma$ (e.g., Hunt 2003), $L_{host} - L_{AGN}$ (Vanden Berk et al. 2006), or color-color diagnostics (e.g., Grewing et al. 1968; Sandage 1971; Elvis et al. 2012) to account for the host contribution. Considering the uncertainty and large scatter in each of these scaling relations, the physical properties of the AGN derived from their analysis may not be robust.

Like most modern SED fitting codes, ARXSED implements a self-consistent approach to dust attenuation, in which the intrinsic SED of radio-loud quasars is appropriately corrected for the reddening and absorption occurring in the torus, the host galaxy, and along the line of sight in the Milky Way.

The main limitations of our approach are a lack of reliable photometry. Several sources in our sample (e.g., 3C 325, and 4C 16.49) lack reliable visible-UV photometry and/or have very few data points, leaving their accretion disk parameters poorly constrained.

ARXSED uses the thermal visible-to-X-ray continuum fitting (Zhang et al. 1997) technique to constrain the SMBH and the accretion disk properties. Constraining the accretion disk parameters without observations around the peak of the thermal continuum is challenging. The peak of the accretion disk is sensitive to the BH mass, Eddington ratio, and spin (see Figure 1); therefore, not having good constraints results in larger uncertainties. To accurately determine the peak of this thermal continuum (occurring around 100–1000 Å rest frame for SMBHs), we require far-UV (FUV) observations from space (e.g., the Cosmic Origins Spectrograph on HST), and soft X-ray data contributing to the high-energy part of the thermal continuum.

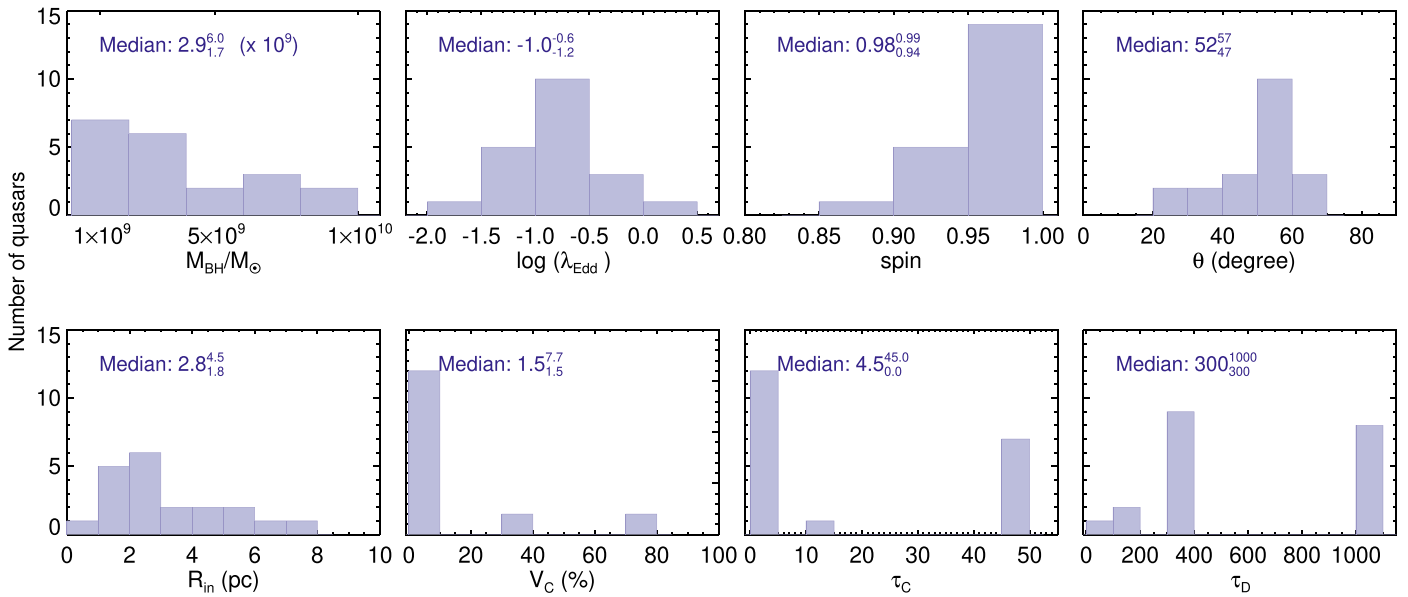


Figure 4. The distribution of the physical properties of the AGN derived from the accretion disk and the torus fits for our 3CRR quasars, along with the median values in each case and their associated 25th (subscript) to 75th (superscript) percentile ranges.

Another advantage of ARXSED is that it implements multicomponent radio models that account for a steepening or cutoff due to the aging of the electron populations. We find that a single power law ($L_{\nu} \propto \nu^{\alpha}$) cannot adequately model the radio emission when compact structures like cores and hot spots are present. In addition, long-wavelength radio photometry usefully constrains the nonthermal radiation from the radio structures at shorter wavelengths. However, a lack of submillimeter data and high-S/N Herschel observations may result in an underestimation of the nonthermal contamination in some cases (e.g., 3C 204) and a corresponding overestimate of SFR.

Given a large number of parameters and diverse data quality, we apply self-consistency checks (e.g., tie the inclination angle of the torus and accretion disk) and use published information (e.g., M_{BH} estimates from emission lines) as priors to the SED fits. However, similar to any SED fitting code, the best-fit SEDs are not unique, and derived parameters may be degenerate with one another. We also note that AGN variability, in particular at radio and visible-UV wavelengths, can bias our SED fits, and impact the physical parameters constrained from the model. To minimize the impact of variability at different wavelengths, we only kept the observations that were close to each other (1) in flux and (2) in observing time.

ARXSED is based on the assumption that the photometry is dominated by the radiation from the AGN at most wavelengths (except for the FIR; see Section 3.4); therefore, we may underestimate the stellar mass in some sources. Also, in sources with small inclination angles (3C 245 and 3C 287; see Table 6) beamed nonthermal emission at IR-visible-UV wavelengths, unaccounted for in our modeling, adds uncertainty to the derived host galaxy properties. We will discuss the results and the limitations of our technique for SFR and stellar mass measurements in detail in a following paper (Azadi et al. 2023, in preparation).

5.2. Physical Properties of the SMBHs and Dusty Tori in 3CRR Quasars

The distributions of the SMBH, torus, and accretion disk properties derived from the SED fits for our 3CRR quasars are shown in Figure 4, along with the median values in each case. The BH mass, Eddington ratio, and spin are constrained by the best-fit accretion disk (see Table 6). The inner radius of the torus, the volume filling factor, the optical depths of the dust clouds, and the homogeneous dusty disk are constrained by the torus model. The inclination angle (measured from the pole) is the average value from the best-fit torus and the accretion disk.

The average BH mass (and the standard deviation) of the quasars in our sample is $(3.7 \pm 2.7) \times 10^9 M_{\odot}$. Our BH masses are obtained from the best-fit accretion disk templates, while the templates are built based on prior mass estimates from broad C IV $\lambda 1548$ or Mg II $\lambda 2800$ emission lines (Section 3.1.1) allowing the mass to vary within ± 1 dex of the initial estimates (see Table 3). Using C IV $\lambda 1548$, Mg II $\lambda 2800$, or H β $\lambda 4863$, McLure et al. (2006) estimated M_{BH} for 18 out of 20 quasars in our sample (except for 3C 318 and 3C 325) and obtained an average of $(3.8 \pm 2.9) \times 10^9 M_{\odot}$. Indeed our estimates of the 3CRR BH masses are consistent with the BH mass estimates of the non-3C radio-loud AGNs at similar redshifts (e.g., Liu et al. 2006) but slightly higher than those at lower redshifts (e.g., Coziol et al. 2017). Recently, Collinson et al. (2015, 2017) investigated the intrinsic NIR to X-ray SEDs of 11 radio-quiet quasars at $1.6 < z < 2.2$ and using the H α $\lambda 6565$ line estimated an average BH mass of $(1.5 \pm 1.4) \times 10^9 M_{\odot}$, which overlaps with the mass of the BHs in our sample. Consistently, with a larger sample at $z < 0.5$, McLure & Dunlop (2002) found that radio-loud quasars have larger BH masses than their radio-quiet counterparts, although with a large overlap.

The average quasar $\log(\lambda_{\text{Edd}})$ obtained for our sample is -0.87 ± 0.41 using the QSOSED templates of Kubota & Done (2018). However, a lack of the FUV and soft X-ray data can bias the measurements toward more massive black holes and/or lower Eddington ratios (Section 3.1.1). Adopting the SMBH

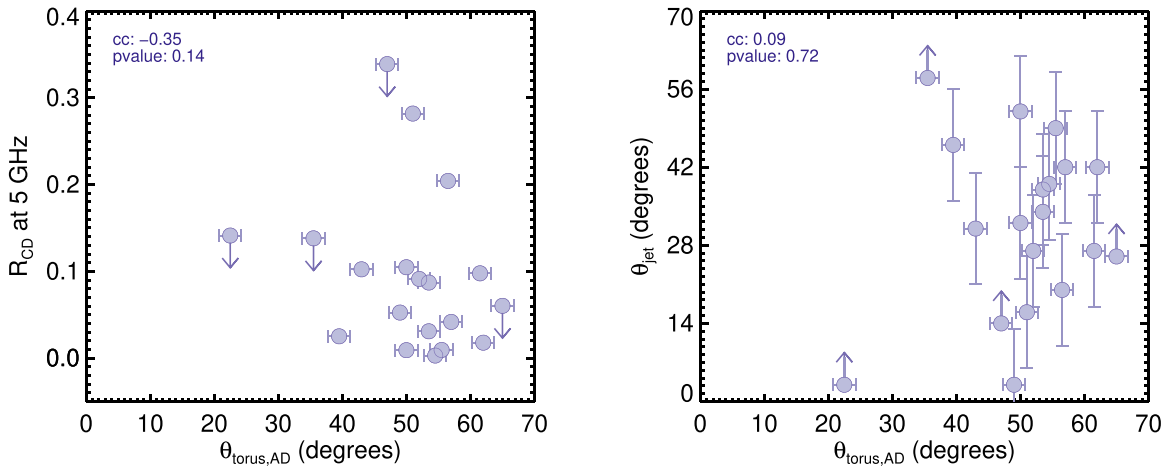


Figure 5. Left: the relation between the radio-core dominance R_{CD} and the average inclination angle of the torus and accretion disk. Right: the relation between the jet inclination angle and the average inclination angle of the torus and accretion disk. The correlation coefficient and its significance level are reported in each panel. For a better illustration, we removed 3C 245, which is an outlier with an R_{CD} of ~ 1.95 .

masses from McLure et al. (2006), and the bolometric correction from Heckman et al. (2004) for estimating L_{bol} from $L_{[\text{O III}]}$, recently Daly (2019) estimated the average $\log \lambda_{\text{Edd}}$ for 15 of the quasars in our sample to be -0.32 ± 0.42 . Given the scatter in the average values, the lower $\log(\lambda_{\text{Edd}})$ in our sample may be attributed to a different methodology used in estimating the Eddington ratio. Adopting the OPTXAGNF accretion disk model of Done et al. (2012), Collinson et al. (2015) estimated an average of $\log(\lambda_{\text{Edd}})$ of 0.02 ± 0.57 for radio-quiet quasars at similar redshift. Coziol et al. (2017) with a large sample of radio-quiet and loud sources at $z < 0.3$ found comparable Eddington ratios for the two populations. Overall, we find a lower Eddington ratio than radio-quiet sources at similar redshifts, with some overlap. But the fact that our best-fit accretion disk model is mostly driven by visible-UV photometry may result in an underestimation of the Eddington ratio (by moving the peak of accretion disk SED to lower frequencies; see Figure 1).

Another parameter estimated from our accretion disk modeling (i.e., thermal continuum fitting) is the SMBH spin. Although the continuum fitting method can estimate the spin of stellar-mass BHs, its application to AGNs can be more challenging. In AGNs, the inner accretion disks are relatively cool ($T \sim 10^5$ K), with the bulk of the thermal emission occurring in the far-or-extreme UV regime, which is hard to observe from the ground. However, recent studies of SMBHs with well-constrained masses found that spins estimated with the thermal continuum fitting method are in good agreement with estimates from reliable techniques such as the X-ray reflection technique (e.g., Capellupo et al. 2016). The average spin of the quasars estimated from the best-fit accretion disk is 0.97 ± 0.04 . Adopting the OPTXAGNF accretion disk model (Done et al. 2012), Collinson et al. (2017) found their radio-quiet sample quasars have spins < 0.9 . While radio-quiet quasars are expected to have lower spin compared to radio-loud sources, they still may have high spin values (see Brenneman & Reynolds 2006). Adopting the Blandford & Znajek (1977) framework in which the BH spin is related to the magnetic field, Daly (2019) estimated the spin of 750 SMBHs and, for the 15 quasars included in our sample, found an average spin of 0.99 ± 0.01 (see also Daly 2011).

The best-fit torus parameters indicate low obscuration, consistent with Type 1 nature of our sources. Indeed all of

the sources with a high filling factor in Table 6 have clumps with negligible optical depth. Also, the negligible optical depth of the clumps in seven out of 20 quasars in our sample (Table 6) indicates that the primary source of torus obscuration is dust in the toroidal disk rather than the clumps. For red quasars (3C 14/190/212/325), the obscuration of the visible-UV emission from the accretion disk is more pronounced (Figure 3), as expected.

The average inclination angle (measured from the pole) obtained from the best-fit torus and accretion disk is $49^\circ \pm 12^\circ$, which is consistent with other studies of nonblazar radio-loud (broad-lined) AGNs (e.g., Willott et al. 2000; Arshakian 2005; Marin & Antonucci 2016). Barthel (1989) found an average inclination angle of 31° for 3CRR quasars at $z < 1$ (estimated from R_{CD}), and 45° as the division between quasars and narrow-line radio galaxies, using the jet inclination angle. We present the inclination angle from the best-fit SED (average of the torus and accretion disk) in Figure 4, while the average viewing angle from the R_{CD} in our sample is $\sim 33^\circ$ (including the limits). We note that our sample (i) does not include blazars,¹⁶ (ii) includes sources with potential nonthermal contamination from the radio structures at IR (e.g., 3C 43), so that the shape of their IR SED (and consequently the best-fitted torus model) is affected by that, (iii) includes red quasars for which, to replicate their IR SED, we need torus templates with higher dust content and/or larger inclination angle. Indeed, all of the sources with torus inclination angle $> 60^\circ$ in our sample are either red quasars (3C 14/190/212/325) or potentially have more nonthermal emission at IR wavelengths than what our model predicts (3C 43/212). We discuss the discrepancies between radio and accretion disk/torus measurements below in Section 5.3.

5.3. The Orientation of 3CRR Quasars

In Figure 5 we investigate the relation of the radio-core dominance, R_{CD} (Section 3.1.3), at 5 GHz and the average inclination angle of the torus and accretion disk obtained from our best fit, as well as the relation between the jet and torus/

¹⁶ Our sample is complete in radio orientation, which means that if there was a 3CRR blazar within this redshift range, it would be included. However, none of our sources have inclination angle $< 20^\circ$.

accretion disk inclination angles. In each panel, we report the correlation coefficient and its significance level based on the `r-correlate`¹⁷ routine in IDL. For better illustration, we removed 3C 245, which is an outlier in our sample with a core contribution of 66% and R_{CD} of 1.95.

We do not find any statistically significant relation between the two parameters in either of the two panels of Figure 5 after removing 3C 245 (with 3C 245, we find $cc = -0.44$, p -value = 0.05 in the left panel). The right panel of Figure 5 shows the relationship between the radio jet inclination angle (taken from Marin & Antonucci 2016; see Table 5) and the average torus/accretion disk inclination angle. Our results indicate that while the jet falls inside the opening angle of the torus (for most of our sources), the orientation of these structures does not always align.

At first glance, the lack of a statistically significant correlation between the parameters in Figure 5 seems to be inconsistent with the unification model in which the flux of the core component decreases as the inclination angle increases. However, there are several factors contributing to these discrepancies. As noted in Section 5.2, the shape of the IR SED (consequently the best-fit torus) is affected by the potential nonthermal component in some sources (e.g., 3C 43/212). Additionally, we speculate that changes in accretion disk/torus orientation after jet launching may ruin any alignments between the two (although this may not lead to the systematic difference seen in Figure 5). Some studies find that a large misalignment between the jet and accretion disk ($>45^\circ$) may tear the disk apart into rings and lead to rapid accretion (e.g., Nealon et al. 2015; Combes 2021) and consequently a different SED. A more definitive study will be carried out when we include the radio galaxies, which will extend the range of orientation.

We also examined the relation between R_{CD} and all of the other torus parameters (e.g., filling factor, and the optical depth of the clouds or disk) and the accretion disk parameters and did not find any significant correlation. Given the limited range of R_{CD} of the quasars in our sample (~ 0 –0.4 without 3C 245), in order to see the variation of the radio-core dominance and obscuration with the inclination angle, we need to include the edge-on sources. This will be addressed in a later paper, in which we will also compare our SED fits with the clear orientation dependence of the X-ray obscuration in this sample (Wilkes et al. 2013).

5.4. Comparisons with the Literature on the SED Fitting of 3CR Sample at $1 < z \lesssim 2$

The SED decomposition of 3CR radio sources at different redshifts and wavelengths has been the subject of several studies (e.g., Drouart et al. 2014; Podigachoski et al. 2015, 2016b; Westhues et al. 2016), but these had mostly a limited wavelength range. Podigachoski et al. (2015) investigated 1–1000 μm SEDs of 3CR quasars and radio galaxies at $1 < z \lesssim 2$ (our parent sample) by fitting the AGN and host galaxy components simultaneously. To model the radiation from the torus, they use the Hönig & Kishimoto (2010) clumpy torus model with a modified blackbody component to describe the emission from hot dust in the torus. To model the host

galaxy component, they use a modified blackbody at FIR wavelengths.

We compared the SEDs of all of our sources with those from Podigachoski et al. (2015) to identify any discrepancies between the physical parameters obtained from the two fitting procedures. As noted in Section 3.1.2, in the Siebenmorgen et al. (2015) torus model, fluffy dust grains that are larger than the standard ISM are adopted, which can survive closer to the BHs, resulting in stronger NIR radiation as well as more pronounced FIR/submillimeter emission. The torus is the dominant source of radiation in our sources in the ~ 2 –30 μm regime, which roughly translates to 100–2000 K dust temperature, while the host galaxy peaks at ~ 60 –100 μm wavelengths (except for 3C 191/268.4) resulting in dust temperatures ~ 25 –50 K. While the host galaxy dominates at FIR wavelengths, the composition of the dust grains and the clumpy structure in our torus model results in more contribution from the torus at FIR wavelengths than Podigachoski et al. (2015). This is particularly noticeable in 3C 190, resulting in a significantly lower estimated SFR (from 470 M_\odot/yr in Podigachoski et al. 2015 to 257 M_\odot/yr from ARXSED). However, this is not the case for 3C 191 and 3C 268.4, in which the torus is dominant at FIR wavelengths.

Also, Podigachoski et al. (2015) considered the host galaxy emission only at FIR wavelengths while our host galaxy model covers UV to radio wavelengths (although it is not the dominant source of radiation in most of these bands). Another difference is the way upper limits are treated in the two models. Podigachoski et al. (2015) treated the upper limits (especially at 70, 160, and 250 μm) as detections during the fit and report the SFR estimated from these bands as upper limits, while we do treat them as upper limits. Finally, unlike ARXSED, Podigachoski et al. (2015) did not consider nonthermal radiation from the radio structures in the submillimeter/FIR bands. Overall, these differences result in lower SFR estimates from our fitting procedure. We will discuss the host galaxy properties (e.g., SFR, stellar mass) and discrepancies with Podigachoski et al. (2015) fully in a future paper.

Podigachoski et al. (2016a) improved upon the approach of Podigachoski et al. (2015) by adopting the Siebenmorgen et al. (2015) torus model and the PÉGASE SED model (Fioc & Rocca-Volmerange 2019) for the host galaxies, while still limiting to 1–1000 μm . However, their improved SED model was only run for 12 NLRG of the Podigachoski et al. (2015) sample sources, which are therefore not directly comparable to our sources.

5.5. Nonthermal Radiation at Observed Millimeter to FIR Wavelengths

Figure 6 illustrates the fraction of nonthermal radiation in our sample calculated at millimeter to FIR observed wavelengths. The best-fit radio model, along with the host galaxy and the torus, is the main component contributing to these wavelengths. Figure 6 shows at 1.25 mm (observed-frame), the total emission is dominated by the radio structure, while at FIR, the torus and the host galaxies are dominant. Our model predicts six sources (out of 20) have minimal synchrotron contribution at 1.25 mm. These are the quasars with a radio emission cutoff that occurs at wavelengths longer than 1.25 mm. Figure 6 also shows that the emission from dust (host galaxy and torus) dominates the synchrotron emission at 450 μm (observed-frame). However, in three of our sources

¹⁷ `r-correlate` computes the Spearman’s rank correlation coefficient (cc) and the significance of its deviation from zero (p -value). A correlation is considered significant if the p -value < 0.05 . In this case, it is unlikely for the correlation to have occurred by accident.

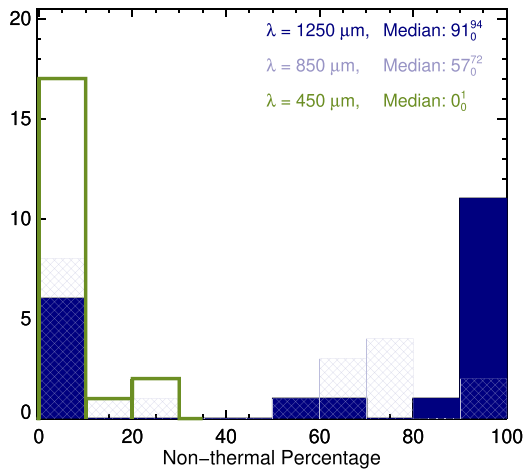


Figure 6. The percentages of nonthermal emission originating from the radio structures at different observed wavelengths. At 1250 μm , the radio component is dominant in the majority of our sources, while at FIR, a combination of the host galaxy and torus dominates. At 850 μm , the thermal emission from dust and nonthermal emission from the radio structures have comparable contributions.

(3C 190/191/268.4), there remains $\sim 20\%$ contribution from the radio structures at 450 μm .

At 850 μm (observed-frame), the thermal emission from the dust and nonthermal emissions from the radio structures are comparable. This implies the submillimeter-based SFR in radio-loud quasars should be calculated after removing potential contamination from radio structures. While in a few of our sources (i.e., 3C 212/245), the 850 μm photometry is dominated by the core contribution, in others the source of the emission, whether from extended structures/lobes or the interaction of the radio structures with the star-forming gas, is not clear. Further observations with a millimeter-wave interferometer are required to understand the nature of submillimeter radiation in these sources.

In addition, there are two sources in Figure 6 (3C 14/186) with comparable thermal and nonthermal emission at 1.25 mm. While 3C 14 has the most extended jet in our sample, 3C 186 is a CSS. However, the shape of the radio spectrum of 3C 186 may suggest that it is confined by a dense environment rather than being young (e.g., Fanti et al. 1995; Hilbert et al. 2016).

Haas et al. (2006) observed seven quasars from our sample (along with four other sources) and found evidence for the synchrotron nature of the observed 1.25 mm and 850 μm radiation. Consistent with Haas et al. (2006), our findings do not confirm earlier results (e.g., Willott et al. 2002) that found the 850 μm emission of quasars at $z \sim 1.5$ is dominated by the thermal emission from dust.

5.6. The Median SED of 3CRR Quasars

Figure 7 presents the median AGN SED (left) and the medians for the individual components (right) in our study. The shaded region around each component shows 25th–75th percentile ranges. Because the number of measurements between the radio and FIR is small, the scatter around the median is significantly larger in these bands. The gray curve (in the left panel) indicates the median SED of the radio-loud quasars in Elvis et al. (1994) normalized at 1.5 μm , and the dotted parts indicate regions with few or no data available in the Elvis et al. (1994) sample. The dotted–dashed curve (in the

right panel) is the median SED of Podigachoski et al. (2015). The median SED of Elvis et al. (1994) was obtained from 18 X-ray-bright radio-loud quasars at $z < 0.8$ after subtracting the host galaxy contribution. The median SED of Podigachoski et al. (2015) was obtained from a sample of 25 3CR radio-loud quasars at $1 < z \lesssim 2$ (our parent sample) using the SED components described in Section 5.4.

The median SED of the Elvis et al. (1994) radio-loud quasars covers a similarly broad frequency range and is qualitatively in agreement with our median SED. However, there are differences between the two curves at some specific bands. Elvis et al.’s (1994) sample has a lower redshift, given the nature of their selection (X-ray bright), but they can still be as luminous as our quasars at X-ray wavelengths. The slope of the X-ray power law in our sample is softer than that of Elvis et al. (1994), which could be either due to the way the two samples are selected (radio-selected versus X-ray selected) and/or the presence of a stronger radio-linked X-ray component in our sample (see also Shang et al. 2011). Indeed, Elvis et al.’s (1994) sources, despite being radio-loud, are much less luminous than our sources at radio bands. Elvis et al.’s (1994) IR observations were limited to IRAS wavelengths, while ours extend to longer wavelengths, and our sources, among the most luminous radio sources known, are ~ 1.7 times more luminous at 1–100 μm .

Another noticeable difference is the much steeper FIR/submillimeter slope (in $\log(\nu) - \log(\nu L_\nu)$ space). Indeed the Elvis et al. (1994) sample lacks the data required to constrain the SED at these wavelengths (also see Shang et al. 2011). Overall, considering the differences at radio and visible-UV wavelengths, the Elvis et al. (1994) median SED does not represent the average behavior of luminous radio-selected AGNs at $z > 1$.

Figure 7 (right) shows the median SED of the quasars (and their host galaxies) from Podigachoski et al. (2015). Given the scatter in the Podigachoski et al. SEDs (0.5–1 dex, not shown for clarity), their median SED is generally consistent with ours. One notable difference is the redder and brighter FIR peak relative to our sample. This may be due to the difference in the torus models, i.e., the larger grains adopted in ARXSED, which results in stronger FIR radiation from the torus and consequently less-pronounced emission from the host galaxy. We also note that ARXSED subtracts the nonthermal radiation from radio structures in the submillimeter/FIR, which can contribute to a fainter FIR peak.

There have been many attempts to derive the average SED of quasars (e.g., Richards et al. 2006; Shang et al. 2011, among others). Richards et al. (2006) studied a sample of SDSS quasars, mostly from FIR-to-X-ray (with an additional eight radio-loud quasars) data, and presented their median SEDs. At X-ray bands, our sources are brighter than those of Richards et al. (2006), which could be either due to the difference between the SDSS and 3CRR sample or could be attributed to a stronger radio-linked X-ray emission in our sample. At submillimeter/FIR wavelengths, the Richards et al. (2006) SEDs have a flatter slope ($\log(\nu) - \log(\nu L_\nu)$ space) than ours (and Elvis et al. 1994) possibly due to the lack of data at these wavelengths, or the smaller number of sources.

Shang et al. (2011) presented the median radio to X-rays SED of a sample of 85 (27 radio-quiet and 58 radio-loud) optically bright, nonblazar quasars. Rather than using detailed SED models, Shang et al. (2011) used H-band photometry as a

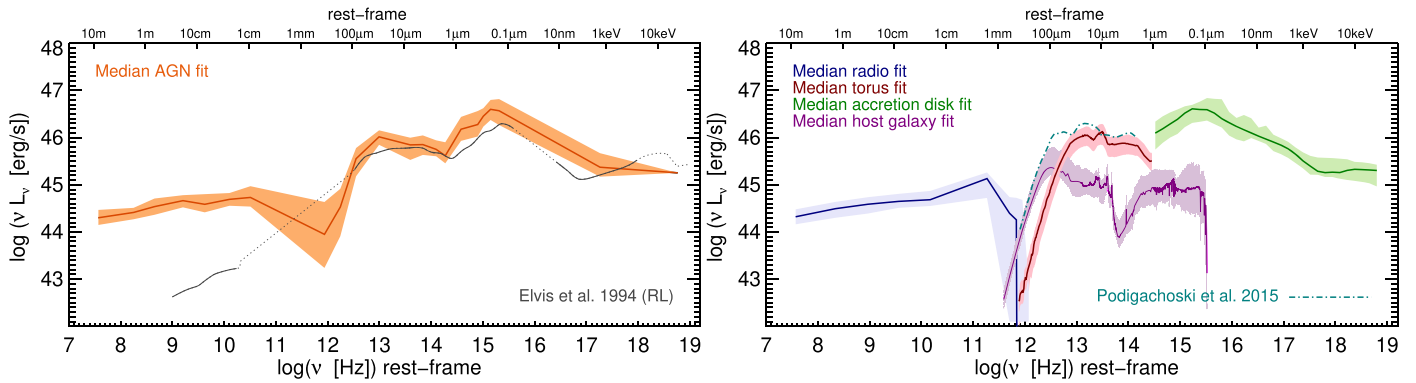


Figure 7. Left: the median SED of the AGN fits in our sample. The gray curve shows the median SED of the radio-loud quasars in Elvis et al. (1994) normalized at $1.5 \mu\text{m}$. The dotted gray curve indicates regions with few or no data available in the Elvis et al. (1994) sample. Right: the median SED of each of the components used in this study. The dotted-dashed curve is the median SED of Podigachoski et al. (2015), which includes the AGN and host galaxy components combined. The shaded region around each component indicates the 25th–75th percentile ranges. The small number of photometric measurements between the radio and FIR bands results in a larger scatter around the median in these bands.

proxy of the host galaxy contribution and corrected the photometry at other wavelengths accordingly. At X-rays, our findings are overall consistent (given that their sample includes luminous radio sources at comparable redshifts). Shang et al. (2011) found more variation in the SED than Elvis et al. (1994) and Richards et al. (2006) by including FIR observations.

In summary, our findings are qualitatively consistent with the literature. However, we provide more detailed features in the shape of the median SED by including Herschel and millimeter/submillimeter photometry. Additionally, we present the median SED using the best-fit model for each component derived using state-of-the-art models in the literature (i.e., torus, accretion disk). To obtain the various components, we tie them to each other in a physically meaningful way and compare our fits with the observations at different wavelengths for individual sources as a sanity check. Another advantage of our median SED is detailed modeling of the host galaxy emission, which all of the studies above lack.

6. Summary

In this study, we present a state-of-the-art AGN radio-to-X-ray SED model (ARXSED) that simultaneously fits AGNs and the host galaxy components. Fitting at radio wavelengths requires four models to account for radiation from the lobes as well as compact radio structures such as radio cores and hot spots (where a superposition of multiple self-absorbed components makes the shape of the spectrum more complex). Additionally, the model accounts for a steepening or cutoff due to the aging of the electron populations. Emission from the torus is fitted by the two-phase torus model of Siebenmorgen et al. (2015) in which the dust can be distributed in a homogeneous disk, a clumpy medium, or a combination of both. The visible-UV-X-ray radiation from the accretion disk is fitted with the QSOSED model developed by Kubota & Done (2018). The emission from the host galaxy is fitted using an underlying component from UV to radio wavelengths (MAGPHYS da Cunha et al. 2008, 2015).

Using ARXSED, we fit the radio-to-X-ray SED of a sample of 20 radio-loud quasars from the 3CRR sample at $1 < z \lesssim 2$. The 3CRR sample includes low-frequency radio-selected AGNs and so is unbiased in terms of orientation and dust obscuration. Hence, the distribution of their orientation angles can be predicted. We have compiled the SED by combining

archival multifrequency radio observations, recent SMA/ALMA observations, Herschel, WISE, Spitzer, 2MASS, UKIRT, SDSS, XMM-Newton, and Chandra for our analysis (Section 2). In order to obtain the intrinsic SED of the AGNs in our sample, we correct the photometry for the reddening and absorption in the host galaxy, the Milky Way, as well as the dusty torus (Section 3.3). Our SED models successfully reproduce the observed photometry and constrain the parameters describing the structures surrounding SMBHs at $z > 1$. Given the large number of parameters, diverse data quality, and possible variability, which may bias our SED fits, we apply priors to the fits based on independent measurements of parameters such as M_{BH} from the literature. This helps to ensure consistency of the SED fitting results, which otherwise may not be unique.

In this paper, we present the fitting results for individual sources (Section 4.1) and the physical properties of the AGN components derived from our modeling (Section 5.2). Our main findings are as follows:

1. A simple power law ($L_\nu \propto \nu^\alpha$) is unable to replicate the radio emission from our sources when complex radio structures (i.e., lobes, jets, cores, and hot spots) are present (Section 4.1).
2. ARXSED predicts that nonthermal emission from the radio structures contributes 91%–57% to the 3CRR quasars SED between 1.25 mm and $850 \mu\text{m}$. It is important to subtract this source of contamination when broadband photometry is used to estimate host galaxy properties such as dust mass and SFR (Section 5.5).
3. The median properties of the best-fit torus parameters and their associated 25th–75th percentile ranges are: the inner radius of the torus, $R_{\text{in}} = 2.8_{1.8}^{4.5}$ (pc), the filling factor of the clumps, $V_{\text{C}} = 1.5_{1.5}^{7.7}$ (%), the optical depth of the clumps, $\tau_{\text{C}} = 4.5_{0.0}^{45.0}$, and the optical depth of the homogeneous disk, $\tau_{\text{D}} = 300_{300}^{1000}$ (Section 5.4).
4. The median properties of the best-fit accretion disk parameters and their associated 25th–75th percentile ranges are as follows: mass of the BH, $M_{\text{BH}}/M_{\odot} = 2.9_{1.7}^{6.0} (\times 10^9)$, the logarithm of Eddington ratio $\log(\lambda_{\text{Edd}}) = -1.0_{-1.2}^{-0.6}$, and the dimensionless spin parameter $a(\equiv Jc/GM_{\text{BH}}^2) = 0.98_{0.94}^{0.99}$. The SMBH properties estimated by ARXSED agree with those extracted

using emission-line techniques in the literature for similarly defined samples (Section 5.4).

5. We find the median (and associated 25th–75th percentile range) inclination angle of $52_{27}^{57}^\circ$ from the best-fit torus/accretion disk, while the average inclination angle of the radio jets reported in the literature for our sample is $33^\circ \pm 14^\circ$. We find that the inclination angle from the torus/accretion disk is not the same as the radio jet. This could be due to an underlying nonthermal contribution from radio structures that changes the shape of the SEDs at shorter wavelengths (affecting the best-fit torus and accretion disk models) and/or the presence of red quasars in our sample. It is also plausible that this misalignment occurs after the jets are launched (Section 5.3). Additionally, we note that the quasars in our sample have a limited range of radio-core dominance, R_{CD} (and jet inclination). To investigate the relation of the jet inclination with the torus/accretion disk parameters, edge-on sources with a wider range of R_{CD} should be considered as well (Section 5.3).
6. We present the median intrinsic SED of the radio-loud quasars at $1 < z \lesssim 2$. Our median SED self-consistently covers the gap in observations and provides more detailed features in the shape of the SED compared to the literature. We find that the median SED of Elvis et al. (1994), obtained based on a sample of radio-loud quasars at $z < 1$, does not describe the SEDs of luminous, radio-selected AGNs at $z > 1$. The difference between the two median SEDs could be due to sample selection, redshift/luminosity, and/or observation limitations (Section 5.6).

We thank the referee for providing positive comments and constructive advice, which helped improve the paper. Support for this work was provided by the National Aeronautics and Space Administration and the Chandra X-ray Center (CXC), which is operated by the Smithsonian Astrophysical Observatory and on behalf of the National Aeronautics Space Administration under contract NAS8-03060 (BJW, MAz,JK). Additional support was provided by NASA NuSTAR grant No. 80NSSC21K0058 (JK).

The scientific results in this article are based significantly on observations made by the Chandra X-ray Observatory (CXO). This research has made use of data obtained from the Chandra Data Archive.

This research has made use of data provided by the National Radio Astronomy Observatory, which is a facility of the National Science Foundation operated under a cooperative agreement with Associated Universities, Inc., and data from the

Sloan Digital Sky Survey (SDSS). Funding for the SDSS and SDSS-II has been provided by the Alfred P. Sloan Foundation, the Participating Institutions, the National Science Foundation, the U.S. Department of Energy, the National Aeronautics and Space Administration, the Japanese Monbukagakusho, the Max Planck Society and the Higher Education Funding Council for England. The SDSS website is <http://www.sdss.org/>. The SDSS is managed by the Astrophysical Research Consortium for the Participating Institutions. The Participating Institutions are the American Museum of Natural History, Astrophysical Institute Potsdam, University of Basel, University of Cambridge, Case Western Reserve University, University of Chicago, Drexel University, Fermilab, the Institute for Advanced Study, the Japan Participation Group, Johns Hopkins University, the Joint Institute for Nuclear Astrophysics, the Kavli Institute for Particle Astrophysics and Cosmology, the Korean Scientist Group, the Chinese Academy of Sciences (LAMOST), Los Alamos National Laboratory, the Max-Planck-Institute for Astronomy (MPIA), the Max-Planck-Institute for Astrophysics (MPA), New Mexico State University, Ohio State University, University of Pittsburgh, University of Portsmouth, Princeton University, the United States Naval Observatory, and the University of Washington.

This research is based on observations made by Herschel, which is an ESA space observatory with science instruments provided by European-led Principal Investigator consortia and with important participation from NASA. This work is based in part on observations made with the Spitzer Space Telescope, which was operated by the Jet Propulsion Laboratory, California Institute of Technology under a contract with NASA.

We acknowledge the use of Ned Wright’s calculator (Wright 2006) and NASA/IPAC Extragalactic Database (NED), operated by the Jet Propulsion Laboratory, California Institute of Technology, under contract with the National Aeronautics and Space Administration.

We acknowledge the use of IRAF, which is distributed by the National Optical Astronomy Observatories, and operated by the Association of Universities for Research in Astronomy, Inc., under contract to the National Science Foundation.

Appendix

Tables A1, A2, and A3 below present high-, medium-, and low-frequency radio data used in the SED analysis in this study with their references. The flux densities are in janskys.

Table A1
High-frequency Radio Data

Name	30 (GHz)	90 (GHz)	31.4 (GHz)	14900 (MHz)	10700 (MHz)	8870 (MHz)	8400 (MHz)	8085 (MHz)	5000 (MHz)	4.85 (GHz)	2695 (MHz)
3C 9				0.13 ± 0.01 L80	0.22 ± 0.02 L80				0.55 ± 0.05 L80	0.48 ± 0.07 G91	0.98 ± 0.04 L80
3C 14				0.15 ± 0.01 L80	0.22 ± 0.02 L80				0.61 ± 0.03 L80	0.55 ± 0.07 G91	1.02 ± 0.04 L80
3C 43	0.06 ± 0.01 SJ95	0.19 ± 0.04 SJ95		0.45 ± 0.01 L80	0.61 ± 0.04 L80				1.08 ± 0.04 L80	1.17 ± 0.16 G91	1.70 ± 0.04 L80
3C 181				0.20 ± 0.01 L80	0.29 ± 0.02 L80				0.66 ± 0.05 L80	0.68 ± 0.09 G91	1.25 ± 0.04 L80
3C 186					0.08 ± 0.01 L80				0.38 ± 0.05 L80	0.31 ± 0.04 G91	0.59 ± 0.04 L80
3C 190				0.30 ± 0.01 L80	0.36 ± 0.02 L80				0.81 ± 0.06 L80	0.7 ± 0.1 G91	1.40 ± 0.05 L80
3C 191				0.18 ± 0.01 L80	0.23 ± 0.02 L80				0.46 ± 0.06 L80	0.56 ± 0.08 G91	0.96 ± 0.04 L80
3C 204				0.11 ± 0.01 L80	0.16 ± 0.01 L80				0.34 ± 0.03 L80	0.37 ± 0.03 G91	0.51 ± 0.04 L80
3C 205				0.16 ± 0.01 L80	0.23 ± 0.02 L80				0.67 ± 0.04 L80	0.69 ± 0.07 G91	1.12 ± 0.04 L80
3C 208				0.14 ± 0.01 L80	0.23 ± 0.02 L80				0.54 ± 0.05 L80	0.51 ± 0.07 G91	0.96 ± 0.04 L80
3C 212				0.48 ± 0.01 L80	0.50 ± 0.02 L80				0.88 ± 0.04 L80	0.7 ± 0.1 G91	1.43 ± 0.04 L80
3C 245			0.94 ± 0.15 G81	0.85 ± 0.01 L80	0.97 ± 0.04 L80	1.0 ± 0.0 S73			1.38 ± 0.04 L80	1.74 ± 0.24 G91	2.0 ± 0.0 W75
3C 268.4				0.18 ± 0.01 L80	0.24 ± 0.02 L80				0.60 ± 0.03 L80	0.61 ± 0.07 G91	1.07 ± 0.04 L80
3C 270.1				0.44 ± 0.01 L80	0.45 ± 0.02 L80				0.86 ± 0.04 L80	0.88 ± 0.11 G91	1.51 ± 0.04 L80
3C 287	0.12 ± 0.02 SJ95	0.51 ± 0.09 SJ95		1.42 ± 0.03 L80	1.73 ± 0.05 L80			2.20 ± 0.18 C83	3.24 ± 0.06 L80	3.11 ± 0.41 G91	4.65 ± 0.06 L80
3C 318				0.23 ± 0.01 L80	0.32 ± 0.02 L80				0.74 ± 0.03 L80	0.85 ± 0.12 G91	1.34 ± 0.04 L80
3C 325				0.25 ± 0.02 L80	0.39 ± 0.02 L80				0.82 ± 0.04 L80	1.1 ± 0.1 G91	1.86 ± 0.04 L80
4C 16.49									0.32 ± 0.0 W90	0.34 ± 0.05 G91	0.68 ± 0.0 W90
3C 432				0.08 ± 0.01 L80	0.13 ± 0.01 L80				0.31 ± 0.06 L80	0.41 ± 0.06 G91	0.77 ± 0.04 L80
3C 454.0				0.30 ± 0.01 L80	0.39 ± 0.03 L80				0.78 ± 0.03 L80	0.79 ± 0.11 G91	1.22 ± 0.04 L80

Table A2
Medium-frequency Radio Data

Name	1400 (MHz)	750 (MHz)	635 (MHz)	408 (MHz)	365 (MHz)	326 (MHz)	178 (MHz)	160 (MHz)	151 (MHz)	86 (MHz)
3C 9	1.96 ± 0.12 L80	3.89 ± 0.19 L80		7.79 ± 0.32 L81						35.7 ± 1.6 L80
3C 14	1.9 ± 0.1 L80	3.58 ± 0.21 L80		5.85 ± 0.18 L81	6.83 ± 0.09 D96		11.3 ± 1.1 L80			24.4 ± 2.7 L80
3C 43	2.82 ± 0.08 L80	4.28 ± 0.18 L80		6.44 ± 0.52 F74	8.56 ± 0.08 D96		12.6 ± 1.3 L80	16.3 ± 2.4 K81		20.5 ± 4.4 L80
3C 181	2.30 ± 0.69 C98	3.76 ± 0.17 L80		6.73 ± 0.21 L81	7.62 ± 0.16 D96		15.80 ± 0.79 L80			24.2 ± 2.2 L80
3C 186	1.24 ± 0.04 C98	2.74 ± 0.17 L80		5.55 ± 0.11 F85	6.58 ± 0.11 D96		15.37 ± 0.77 L80		15.59 ± 0.07 H93	33.2 ± 2.7 L80
3C 190	2.55 ± 0.07 L80	4.30 ± 0.17 L80		7.63 ± 0.24 L81	9.09 ± 0.09 D96		16.35 ± 0.82 L80			26.8 ± 2.7 L80
3C 191	1.85 ± 0.06 C98	3.44 ± 0.17 L80		7.32 ± 0.32 L81	7.49 ± 0.08 D96		14.17 ± 0.71 L80			34.3 ± 1.6 L80
3C 204	1.30 ± 0.08 L80	2.37 ± 0.06 P66		7.32 ± 0.32 L81	5.49 ± 0.17 D96	7.9	11.45 ± 0.57 L80			29.6 ± 1.1 L80
3C 205	2.39 ± 0.07 L80	3.95 ± 0.18 L80			9.3 ± 0.2 D96		13.7 ± 1.4 L80			39.2 ± 4.4 L80
3C 208	2.36 ± 0.07 C98	4.56 ± 0.17 L80		7.75 ± 0.25 L81	10.33 ± 0.18 D96		20.0 ± 1.0 L80			41.5 ± 2.4 L80
3C 212	2.37 ± 0.07 C98	4.44 ± 0.18 L80		7.01 ± 0.22 L81	8.34 ± 0.15 D96		16.46 ± 0.82 L80			29.8 ± 3.1 L80
3C 245	3.3 ± 0.1 C98	5.06 ± 0.18 L80		8.90 ± 0.37 L81	9.45 ± 0.21 D96		15.70 ± 0.79 L80			27.4 ± 1.1 L80
3C 268.4	1.98 ± 0.06 C98	3.62 ± 0.17 L80		5.69 ± 0.12 F85	6.58 ± 0.12 D96		11.23 ± 0.56 L80			22.4 ± 2.7 L80
3C 270.1	2.73 ± 0.07 L80	5.0 ± 0.1 P66		8.20 ± 0.41 C70	9.74 ± 0.13 D96		14.82 ± 0.74 L80			30.8 ± 2.7 L80
3C 287	7.05 ± 0.21 C90	9.67 ± 0.25 L80		11.94 ± 0.95 C72	14.96 ± 0.28 D96		17.44 ± 0.87 L80	20 ± 3 K81	15.5 ± 0.7 W96	19.4 ± 2.2 L80
3C 318	2.56 ± 0.07 L80	2.69 ± 0.08 C98	4.44 ± 0.18 L80			9.21 ± 0.09 D96		13.41 ± 0.67 L80		13.98 ± 0.64 W96
3C 325	3.56 ± 0.13 C98	6.19 ± 0.19 L80			12.12 ± 0.29 D96		17.0 ± 0.9 L80			33.1 ± 2.7 L80
4C 16.49	1.46 ± 0.05 C98			5.36 ± 0.17 L81	6.3 ± 0.1 D96		10.50 ± 0.84 G67			
3C 432	1.58 ± 0.06 C98	2.90 ± 0.17 L80		6.05 ± 0.15 L81	6.48 ± 0.12 D96		12.0 ± 1.2 L80			21.1 ± 1.9 L80
3C 454.0	2.14 ± 0.07 L80	3.46 ± 0.17 L80		5.65 ± 0.18 L81	6.49 ± 0.05 D96		12.64 ± 0.63 L80			

Table A3
Low-frequency Radio Data

Name	80 (MHz)	74 (MHz)	60 (MHz)	38 (MHz)	26.3 (MHz)	25.0 (MHz)	22.25 (MHz)	20.0 (MHz)	16.7 (MHz)	14.7 (MHz)	12.6 (MHz)	10 (MHz)
3C 9			53.0 ± 7.1 A68	75.5 ± 7.6 L80	99.0 ± 18.0 L80		97.8 ± 16.7 L80					204.0 ± 42.0 L80
3C 14				42.5 ± 8.5 L80	69.0 ± 7.0 L80							
3C 43	23.0 ± 3.0 K81			46.0 ± 9.2 L80	46.0 ± 6.0 L80		69.0 ± 8.3 L80					
3C 181			54.0 ± 4.0 A68	37.8 ± 7.6 L80	57.0 ± 8.0 L80							
3C 186			42.02 ± 3.01 A68	57.8 ± 5.8 L80	54.0 ± 7.0 L80	77.0 ± 24.0 B70	54.1 ± 5.0 L80	61.0 ± 17.0 B70	103.0 ± 35.0 B70	126.0 ± 45.0 B70	120.0 ± 47.0 B70	
3C 190			40.1 ± 8.0	64.0 ± 8.0		71.3 ± 11.7						192.0 ± 42.0 L80
3C 191				56.6 ± 5.7 L80	46.0 ± 8.0 L80		96.6 ± 11.7 L80	120.0 ± 18.0 B69	160.0 ± 32.0 B69	300.0 ± 66.0 B69	380.0 ± 84.0 B69	276.0 ± 66.0 L80
3C 204		26.6 ± 2.7 C07	34.0 ± 3.0 A68	58.9 ± 10.0 H95		101.0 ± 19.2 B70		95.0 ± 19.0 B70	131.0 ± 26.2 B70		380.0 ± 84.0 B70	
3C 205				54.3 ± 5.4 L80	60.0 ± 10.0 L80			88.0 ± 16.7 B70	85.0 ± 16.2 B70	130.0 ± 28.6 B70	147.0 ± 32.3 B70	162.0 ± 36.0 L80
3C 208			42.02 ± 3.01 A68	68.44 ± 6.84 L80	83.0 ± 10.0 L80		67.9 ± 21.7 L80					
3C 212			46.02 ± 4.0 A68				29.9 ± 11.7 L80					
3C 245			34.0 ± 5.0 A68	47.2 ± 4.7 L80	73.0 ± 8.0 L80		64.4 ± 11.7 L80	137.0 ± 57.5 B70	125.0 ± 35.0 B70	132.0 ± 27.7 B70	161.0 ± 45.1 B70	170.4 ± 39.6 L80
3C 268.4		20.7 ± 3.8 M05		36.6 ± 7.3 L80	34.0 ± 8.0 L80							
3C 270.1		30.8 ± 0.0 C04		33.0 ± 6.6 L80	60.0 ± 8.0 L80		60.9 ± 10.0 L80	85.0 ± 30.0 B70	141.0 ± 65.0 B70	210.0 ± 61.0 B70		
3C 287				30.7 ± 6.1 L80		65.0 ± 21.0 B69		120.0 ± 50.4 B69	140.0 ± 61.6 B69	240.0 ± 120.0 B69	320.0 ± 160.0 B69	
3C 318					25.9 ± 7.8 L80	31.0 ± 7.0 L80		37.9 ± 3.3 L80				
3C 325				42.5 ± 4.3 L80								
4C 16.49					42.0 ± 9.0 V75							
3C 432				55.5 ± 11.1 L80	42.0 ± 7.0 L80		65.6 ± 8.3 L80					
3C 454.0			24.0 ± 3.0 A68	31.9 ± 9.6 L80								

References. A68 - Aslanian et al. (1968), B69 - Braude et al. (1969), B70 - Braude et al. (1970), C70 - Colla et al. (1970), C72 - Colla et al. (1972), C73 - Colla et al. (1973), C83 - Condon et al. (1983), C98 - Condon et al. (1998), C04 - Cohen et al. (2004), D96 - Douglas et al. (1996), F74 - Fanti et al. (1974), F85 - Ficarra et al. (1985), G67 - Gower et al. (1967), G81 - Geldzahler & Witzel (1981), G91 - Gregory & Condon (1991), H90 - Hales et al. (1990), H93 - Hales et al. (1993), H95 - Hales et al. (1995), K69 - Kellermann et al. (1969), K73 - Kellermann & Pauliny-Toth (1973), K81 - Kuehr et al. (1981), L80 - Laing & Peacock (1980), L81 - Large et al. (1981), M05 - Mack et al. (2005), P66 - Pauliny-Toth et al. (1966), S73 - Shimmins & Wall (1973), SJ95 - Steppe et al. (1995), S95 - Slee (1995), V75 - Viner & Erickson (1975), W75 - Wills (1975), W90 - Wright & Otrupcek (1990), W96 - Waldram et al. (1996), C07- Cohen et al. (2007).

ORCID iDs

Mojegan Azadi  <https://orcid.org/0000-0001-6004-9728>
 Belinda Wilkes  <https://orcid.org/0000-0003-1809-2364>
 Joanna Kuraszkiwicz  <https://orcid.org/0000-0001-5513-029X>
 Jonathan McDowell  <https://orcid.org/0000-0002-7093-295X>
 Ralf Siebenmorgen  <https://orcid.org/0000-0002-9788-672X>
 Matthew Ashby  <https://orcid.org/0000-0002-3993-0745>
 Mark Birkinshaw  <https://orcid.org/0000-0002-1858-277X>
 Diana Worrall  <https://orcid.org/0000-0002-1516-0336>
 Natasha Abrams  <https://orcid.org/0000-0002-0287-3783>
 Peter Barthel  <https://orcid.org/0000-0002-0106-5776>
 Martin Haas  <https://orcid.org/0000-0002-7284-0477>
 Eileen T. Meyer  <https://orcid.org/0000-0002-7676-9962>

References

- Aird, J., Coil, A. L., Moustakas, J., et al. 2012, *ApJ*, 746, 90
 Akujor, C. E., & Garrington, S. T. 1995, *A&AS*, 112, 235
 Akujor, C. E., Spencer, R. E., & Saikia, D. J. 1991, *A&A*, 249, 337
 Akujor, C. E., Luedke, E., Browne, I. W. A., et al. 1994, *A&AS*, 105, 247
 Aldcroft, T. L., Siemiginowska, A., Elvis, M., et al. 2003, *ApJ*, 597, 751
 Anderson, S. F., Weymann, R. J., Foltz, C. B., & Chaffee, F. H., Jr. 1987, *AJ*, 94, 278
 Arshakian, T. G. 2005, *A&A*, 436, 817
 Aslanian, A. M., Dagkesamanskii, R. D., Kozhukhov, V. N., Malumian, V. G., & Sanamian, V. A. 1968, *Afz*, 4, 129
 Azadi, M., Aird, J., Coil, A. L., et al. 2015, *ApJ*, 806, 187
 Azadi, M., Coil, A. L., Aird, J., et al. 2017, *ApJ*, 835, 27
 Barthel, P., & Versteeg, J. 2019, *Msngr*, 176, 37
 Barthel, P. D. 1989, *ApJ*, 336, 606
 Barthel, P. D., Tytler, D. R., & Thomson, B. 1990, *A&AS*, 82, 339
 Barthel, P., Podgachoski, P., Wilkes, B., & Haas, M. 2017, *ApJL*, 843, L16
 Baskin, A., & Laor, A. 2005, *MNRAS*, 356, 1029
 Becker, R. H., White, R. L., Gregg, M. D., et al. 2000, *ApJ*, 538, 72
 Becker, R. H., White, R. L., Gregg, M. D., et al. 2001, *ApJS*, 135, 227
 Benn, C. R., Vigotti, M., Carballo, R., Gonzalez-Serrano, J. I., & Sanchez, S. F. 1998, *MNRAS*, 295, 451
 Bernhard, E., Mullaney, J. R., Daddi, E., Ciesla, L., & Schreiber, C. 2016, *MNRAS*, 460, 902
 Berta, S., Lutz, D., Santini, P., et al. 2013, *A&A*, 551, A100
 Best, P. N., & Heckman, T. M. 2012, *MNRAS*, 421, 1569
 Best, P. N., Kauffmann, G., Heckman, T. M., et al. 2005, *MNRAS*, 362, 25
 Best, P. N., Von Der Linden, A., Kauffmann, G., Heckman, T. M., & Kaiser, C. R. 2007, *MNRAS*, 379, 894
 Bianchi, S., Guainazzi, M., Matt, G., Fonseca Bonilla, N., & Ponti, G. 2009, *A&A*, 495, 421
 Blandford, R. D., & Königl, A. 1979, *ApJ*, 232, 34
 Blandford, R. D., & Znajek, R. L. 1977, *MNRAS*, 179, 433
 Boquien, M., Burgarella, D., Roehly, Y., et al. 2019, *A&A*, 622, A103
 Braatz, J. A., Wilson, A. S., Gezari, D. Y., Varosi, F., & Beichman, C. A. 1993, *ApJL*, 409, L5
 Braude, S. Y., Lebedeva, O. M., Megn, A. V., Ryabov, B. P., & Zhouck, I. N. 1969, *MNRAS*, 143, 289
 Braude, S. Y., Lebedeva, O. M., Megn, A. V., Ryabov, B. P., & Zhouck, I. N. 1970, *ApL*, 5, 129
 Bremer, M. N., Crawford, C. S., Fabian, A. C., & Johnstone, R. M. 1992, *MNRAS*, 254, 614
 Brenneman, L. W., & Reynolds, C. S. 2006, *ApJ*, 652, 1028
 Bridle, A. H., Hough, D. H., Lonsdale, C. J., Burns, J. O., & Laing, R. A. 1994, *AJ*, 108, 766
 Brotherton, M. S., Tran, H. D., Becker, R. H., et al. 2001, *ApJ*, 546, 775
 Brown, A., Nayyeri, H., Cooray, A., et al. 2019, *ApJ*, 871, 87
 Bruzual, G., & Charlot, S. 2003, *MNRAS*, 344, 1000
 Burns, J. O. 1990, *AJ*, 99, 14
 Calderone, G., Sbarrato, T., & Ghisellini, G. 2012, *MNRAS Lett.*, 425, L41
 Cameron, M., Storey, J. W. V., Rotaciuc, V., et al. 1993, *ApJ*, 419, 136
 Campitiello, S., Celotti, A., Ghisellini, G., & Sbarrato, T. 2021, *A&A*, 656, A96
 Capellupo, D. M., Netzer, H., Lira, P., Trakhtenbrot, B., & Mejía-Restrepo, J. 2016, *MNRAS*, 460, 212
 Chabrier, G. 2003, *PASP*, 115, 763
 Charlot, S., & Fall, S. M. 2000, *ApJ*, 539, 718
 Chiaberge, M., & Marconi, A. 2011, *MNRAS*, 416, 917
 Cleary, K., Lawrence, C. R., Marshall, J. A., Hao, L., & Meier, D. 2007, *ApJ*, 660, 117
 Cohen, A. S., Röttgering, H. J. A., Jarvis, M. J., Kassim, N. E., & Lazio, T. J. W. 2004, *ApJS*, 150, 417
 Cohen, A. S., Lane, W. M., Cotton, W. D., et al. 2007, *AJ*, 134, 1245
 Colla, G., Fanti, C., Ficarra, A., et al. 1970, *A&AS*, 1, 281
 Colla, G., Fanti, C., Fanti, R., et al. 1972, *A&AS*, 7, 1
 Colla, G., Fanti, C., Fanti, R., et al. 1973, *A&AS*, 11, 291
 Collinson, J. S., Ward, M. J., Done, C., et al. 2015, *MNRAS*, 449, 2174
 Collinson, J. S., Ward, M. J., Landt, H., et al. 2017, *MNRAS*, 465, 358
 Combes, F. 2021, in *IAU. Symp. 359, Galaxy Evolution and Feedback Across Different Environments*, ed. T. Storchi Bergmann et al. (Cambridge: Cambridge Univ. Press), 312
 Condon, J. J., Condon, M. A., Broderick, J. J., & Davis, M. M. 1983, *AJ*, 88, 20
 Condon, J. J., Cotton, W. D., Greisen, E. W., et al. 1998, *AJ*, 115, 1693
 Coziol, R., Andernach, H., Torres-Papaqui, J. P., Ortega-Minakata, R. A., & Moreno del Rio, F. 2017, *MNRAS*, 466, 921
 Crummy, J., Fabian, A. C., Gallo, L., & Ross, R. R. 2006, *MNRAS*, 365, 1067
 Cutri, R. M., Nelson, B. O., Kirkpatrick, J. D., Huchra, J. P., & Smith, P. S. 2001, *AAS Meeting*, 198, 33.17
 Czerny, B., Nikolajuk, M., Różańska, A., et al. 2003, *A&A*, 412, 317
 da Cunha, E., Charlot, S., & Elbaz, D. 2008, *MNRAS*, 388, 1595
 da Cunha, E., Walter, F., Smail, I. R., et al. 2015, *ApJ*, 806, 110
 Daly, R. 2011, *MNRAS*, 414, 1253
 Daly, R. A. 2019, *ApJ*, 886, 37
 Davis, S. W., & Laor, A. 2011, *ApJ*, 728, 98
 Done, C., Davis, S. W., Jin, C., Blaes, O., & Ward, M. 2012, *MNRAS*, 420, 1848
 Done, C., Jin, C., Middleton, M., & Ward, M. 2013, *MNRAS*, 434, 1955
 Douglas, J. N., Bash, F. N., Bozyan, F. A., Torrence, G. W., & Wolfe, C. 1996, *AJ*, 111, 1945
 Drouart, G., De Breuck, C., Vernet, J., et al. 2014, *A&A*, 566, A53
 Edelson, R. A., & Malkan, M. A. 1986, *ApJ*, 308, 59
 Efstathiou, A., & Rowan-Robinson, M. 1995, *MNRAS*, 273, 649
 Elvis, M. 2010, in *IAU Symp. 267, Co-Evolution of Central Black Holes and Galaxies*, ed. B. M. Peterson, R. S. Somerville, & T. Storchi-Bergmann (Cambridge: Cambridge Univ. Press), 55
 Elvis, M., Wilkes, B. J., McDowell, J. C., et al. 1994, *ApJS*, 95, 1
 Elvis, M., Hao, H., Civano, F., et al. 2012, *ApJ*, 759, 6
 Fabian, A. C., Celotti, A., & Johnstone, R. M. 2003, *MNRAS*, 338, L7
 Fanaroff, B. L., & Riley, J. M. 1974, *MNRAS*, 167, 31P
 Fanti, C., Fanti, R., Ficarra, A., & Padrielli, L. 1974, *A&AS*, 18, 147
 Fanti, C., Fanti, R., Parma, P., et al. 1989, *A&A*, 217, 44
 Fanti, C., Fanti, R., Dallacasa, D., et al. 1995, *A&A*, 302, 317
 Feltre, A., Hatziminaoglou, E., Fritz, J., & Franceschini, A. 2012, *MNRAS*, 426, 120
 Ferrini, I., Burns, J. O., & Perley, R. A. 1997, *AJ*, 114, 2292
 Ficarra, A., Gruelf, G., & Tomassetti, G. 1985, *A&AS*, 59, 255
 Floc, M., & Rocca-Volmerange, B. 2019, *A&A*, 623, A143
 Foley, A. R., & Barthel, P. D. 1990, *A&A*, 228, 17
 Fritz, J., Franceschini, A., & Hatziminaoglou, E. 2006, *MNRAS*, 366, 767
 Geach, J. E., Smail, I., Moran, S. M., et al. 2011, *ApJL*, 730, L19
 Geldzahler, B. J., & Witzel, A. 1981, *AJ*, 86, 1306
 Georgakakis, A., Clements, D. L., Bendo, G., et al. 2009, *MNRAS*, 394, 533
 Ghisellini, G. 2013, *Radiative Processes in High Energy Astrophysics*, Vol. 873 (Cham: Springer) doi:10.1007/978-3-319-00612-3
 Gierliński, M., & Done, C. 2004, *MNRAS*, 349, L7
 Gower, J. F. R., Scott, P. F., & Wills, D. 1967, *MNRAS*, 71, 49
 Gregory, P. C., & Condon, J. J. 1991, *ApJS*, 75, 1011
 Grewing, M., Demoulin, M.-H., & Burbidge, G. R. 1968, *ApJ*, 154, 447
 Grimes, J. A., Rawlings, S., & Willott, C. J. 2005, *MNRAS*, 359, 1345
 Haardt, F., & Maraschi, L. 1993, *ApJ*, 413, 507
 Haas, M., Chini, R., Müller, S. A. H., Bertoldi, F., & Albrecht, M. 2006, *A&A*, 445, 115
 Haas, M., Willner, S. P., Heymann, F., et al. 2008, *ApJ*, 688, 122
 Hales, S. E. G., Baldwin, J. E., & Warner, P. J. 1993, *MNRAS*, 263, 25
 Hales, S. E. G., Masson, C. R., Warner, P. J., & Baldwin, J. E. 1990, *MNRAS*, 246, 256
 Hales, S. E. G., Waldram, E. M., Rees, N., & Warner, P. J. 1995, *MNRAS*, 274, 47
 Hamann, F. W., Barlow, T. A., Chaffee, F. C., Foltz, C. B., & Weymann, R. J. 2001, *ApJ*, 550, 142

- Hao, H., Elvis, M., Civano, F., et al. 2014, *MNRAS*, **438**, 1288
- Hardcastle, M. J., & Croston, J. H. 2020, *NewAR*, **88**, 101539
- Heckman, T. M., & Best, P. N. 2014, *ARA&A*, **52**, 589
- Heckman, T. M., Kauffmann, G., Brinchmann, J., et al. 2004, *ApJ*, **613**, 109
- Hilbert, B., Chiaberge, M., Kotyla, J. P., et al. 2016, *ApJS*, **225**, 12
- Hönig, S. F., & Kishimoto, M. 2010, *A&A*, **523**, A27
- Hönig, S. F., Kishimoto, M., Tristram, K. R. W., et al. 2013, *ApJ*, **771**, 87
- Hunt, A. M. L. K. 2003, *ApJL*, **589**, L21
- Ishwara-Chandra, C. H., Dwarakanath, K. S., & Anantharamaiah, K. R. 2003, *JApA*, **24**, 37
- Janssen, R. M. J., Röttgering, H. J. A., Best, P. N., & Brinchmann, J. 2012, *A&A*, **541**, A62
- Jester, S. 2005, *ApJ*, **625**, 667
- Kellermann, K. I., & Pauliny-Toth, I. I. K. 1973, *AJ*, **78**, 828
- Kellermann, K. I., Pauliny-Toth, I. I. K., & Williams, P. J. S. 1969, *ApJ*, **157**, 1
- Kellermann, K. I., Sramek, R., Schmidt, M., Shaffer, D. B., & Green, R. 1989, *AJ*, **98**, 1195
- Kellermann, K. I., Condon, J. J., Kimball, A. E., Perley, R. A., & Ivezić, Ž. 2016, *ApJ*, **831**, 168
- Kim, D., & Im, M. 2018, *A&A*, **610**, A31
- Kirkpatrick, A., Alberts, S., Pope, A., et al. 2017, *ApJ*, **849**, 111
- Kishimoto, M., Hönig, S. F., Antonucci, R., et al. 2011, *A&A*, **527**, A121
- Konigl, A. 1981, *ApJ*, **243**, 700
- Kriek, M., van Dokkum, P. G., Labbé, I., et al. 2009, *ApJ*, **700**, 221
- Krügel, E. 2009, *A&A*, **493**, 385
- Krügel, E., & Siebenmorgen, R. 1994, *A&A*, **288**, 929
- Kubota, A., & Done, C. 2018, *MNRAS*, **480**, 1247
- Kuehr, H., Witzel, A., Pauliny-Toth, I. I. K., & Nauber, U. 1981, *A&AS*, **45**, 367
- Kuraszkiewicz, J. K., Green, P. J., Forster, K., et al. 2002, *ApJS*, **143**, 257
- Kuraszkiewicz, J. K., Wilkes, B. J., Hooper, E. J., et al. 2003, *ApJ*, **590**, 128
- Lacy, M., Storrie-Lombardi, L. J., Sajina, A., et al. 2004, *ApJS*, **154**, 166
- Laing, R. A., & Peacock, J. A. 1980, *MNRAS*, **190**, 903
- Laing, R. A., Riley, J. M., & Longair, M. S. 1983, *MNRAS*, **204**, 151
- Lani, C., Netzer, H., & Lutz, D. 2017, *MNRAS*, **471**, 59
- Laor, A., & Davis, S. W. 2014, *MNRAS*, **438**, 3024
- Large, M. I., Mills, B. Y., Little, A. G., Crawford, D. F., & Sutton, J. M. 1981, *MNRAS*, **194**, 693
- Lee, S.-K., Ferguson, H. C., Somerville, R. S., Wiklind, T., & Giavalisco, M. 2010, *ApJ*, **725**, 1644
- Leipski, C., Haas, M., Willner, S. P., et al. 2010, *ApJ*, **717**, 766
- Leja, J., Johnson, B. D., Conroy, C., van Dokkum, P. G., & Byler, N. 2017, *ApJ*, **837**, 170
- Leja, J., Johnson, B. D., Conroy, C., & van Dokkum, P. 2018, *ApJ*, **854**, 62
- Liu, R., Pooley, G., & Riley, J. M. 1992, *MNRAS*, **257**, 545
- Liu, Y., Jiang, D. R., & Gu, M. F. 2006, *ApJ*, **637**, 669
- Lonsdale, C. J., & Barthel, P. D. 1984, *A&A*, **135**, 45
- Lonsdale, C. J., & Barthel, P. D. 1986, *AJ*, **92**, 12
- Lonsdale, C. J., Barthel, P. D., & Miley, G. K. 1993, *ApJS*, **87**, 63
- Ludke, E., Garrington, S. T., Spencer, R. E., et al. 1998, *MNRAS*, **299**, 467
- Mack, K.-H., Vigotti, M., Gregorini, L., et al. 2005, *A&A*, **435**, 863
- Madau, P., & Dickinson, M. 2014, *ARA&A*, **52**, 415
- Mantovani, F., Junor, W., Fanti, R., et al. 1992, *MNRAS*, **257**, 353
- Marin, F., & Antonucci, R. 2016, *ApJ*, **830**, 82
- Markwardt, C. B. 2009, in ASP Conf. Ser. 411, *Astronomical Data Analysis Software and Systems XVIII*, ed. D. A. Bohlender, D. Durand, & P. Dowler (San Francisco, CA: ASP), 251
- McLure, R. J., & Dunlop, J. S. 2002, *MNRAS*, **331**, 795
- McLure, R. J., Jarvis, M. J., Targett, T. A., Dunlop, J. S., & Best, P. N. 2006, *MNRAS*, **368**, 1395
- Middei, R., Bianchi, S., Cappi, M., et al. 2018, *A&A*, **615**, A163
- Mullaney, J. R., Alexander, D. M., Goulding, A. D., & Hickox, R. C. 2011, *MNRAS*, **414**, 1082
- Nealon, R., Price, D. J., & Nixon, C. J. 2015, *MNRAS*, **448**, 1526
- Nenkova, M., Sirocky, M. M., Ivezić, Ž., & Elitzur, M. 2008, *ApJ*, **685**, 147
- Netzer, H., Lutz, D., Schweitzer, M., et al. 2007, *ApJ*, **666**, 806
- Neugebauer, G., Oke, J. B., Becklin, E. E., & Matthews, K. 1979, *ApJ*, **230**, 79
- Novikov, I. D., & Thorne, K. S. 1973, in *Black Holes (Les Astres Occlus)*, ed. C. DeWitt & B. DeWitt (New York: Gordon and Breach), 343
- O'Dea, C. P. 1998, *PASP*, **110**, 493
- Orr, M. J. L., & Browne, I. W. A. 1982, *MNRAS*, **200**, 1067
- Page, M. J., Symeonidis, M., Vieira, J. D., et al. 2012, *Natur*, **485**, 213
- Pauliny-Toth, I. I. K., Wade, C. M., & Heeschen, D. S. 1966, *ApJS*, **13**, 65
- Petrucci, P.-O., Haardt, F., Maraschi, L., et al. 2001, *ApJ*, **556**, 716
- Petrucci, P.-O., Paltani, S., Malzac, J., et al. 2013, *A&A*, **549**, A73
- Petrucci, P.-O., Ursini, F., De Rosa, A., et al. 2018, *A&A*, **611**, A59
- Piconcelli, E., Jimenez-Bailón, E., Guainazzi, M., et al. 2005, *A&A*, **432**, 15
- Pier, E. A., & Krolik, J. H. 1992, *ApJ*, **401**, 99
- Podigachoski, P., Barthel, P. D., Haas, M., et al. 2015, *A&A*, **575**, A80
- Podigachoski, P., Rocca-Volmerange, B., Barthel, P., Drouart, G., & Fioc, M. 2016a, *MNRAS*, **462**, 4183
- Podigachoski, P., Barthel, P. D., Peletier, R. F., & Steendam, S. 2016b, *A&A*, **585**, A142
- Polletta, M., Courvoisier, R. J.-L., Hooper, E. J., & Wilkes, B. J. 2000, *A&A*, **362**, 75
- Polletta, M., Tajer, M., Maraschi, L., et al. 2007, *ApJ*, **663**, 81
- Rees, M. J. 1984, *ARA&A*, **22**, 471
- Reynolds, C. S. 2019, *NatAs*, **3**, 41
- Richards, G. T., Lacy, M., Storrie-Lombardi, L. J., et al. 2006, *ApJS*, **166**, 470
- Rieke, G. H., & Lebofsky, M. J. 1981, *ApJ*, **250**, 87
- Roche, P. F., Aitken, D. K., Smith, C. H., & Ward, M. J. 1991, *MNRAS*, **248**, 606
- Rosario, D. J., Santini, P., Lutz, D., et al. 2012, *A&A*, **545**, A45
- Rovilos, E., Comastri, A., Gilli, R., et al. 2012, *A&A*, **546**, A58
- Rowan-Robinson, M. 1995, *MNRAS*, **272**, 737
- Salvesen, G., Miller, J. M., Cackett, E., & Siemiginowska, A. 2009, *ApJ*, **692**, 753
- Sandage, A. R. 1971, in *Proc. Study Week on Nuclei of Galaxies*, ed. D. J. K. O'Connell (New York: Elsevier), 271
- Sanitt, N. 1976, *MNRAS*, **174**, 91
- Shakura, N. I., & Sunyaev, R. A. 1976, *MNRAS*, **175**, 613
- Shang, Z., Brotherton, M. S., Wills, B. J., et al. 2011, *ApJS*, **196**, 2
- Shangguan, J., Ho, L. C., Bauer, F. E., Wang, R., & Treister, E. 2020, *ApJ*, **899**, 112
- Shen, Y. 2013, *BASI*, **41**, 61
- Shimmins, A. J., & Wall, J. V. 1973, *AuJPh*, **26**, 93
- Siebenmorgen, R., Heymann, F., & Efstathiou, A. 2015, *A&A*, **583**, A120
- Siebenmorgen, R., Voshchinnikov, N. V., & Bagnulo, S. 2014, *A&A*, **561**, A82
- Siebenmorgen, R., Haas, M., Krügel, E., & Schulz, B. 2005, *A&A*, **436**, L5
- Siemiginowska, A., Burke, D. J., Aldcroft, T. L., et al. 2010, *ApJ*, **722**, 102
- Sikora, M., Stawarz, Ł., & Lasota, J.-P. 2007, *ApJ*, **658**, 815
- Slee, O. B. 1995, *AuJPh*, **48**, 143
- Smith, H. E., & Spinrad, H. 1980, *PASP*, **92**, 553
- Spencer, R. E., Schilizzi, R. T., Fanti, C., et al. 1991, *MNRAS*, **250**, 225
- Spinrad, H., Djorgovski, S., Marr, J., & Aguilar, L. 1985, *PASP*, **97**, 932
- Steppe, H., Jeyakumar, S., Saikia, D. J., & Salter, C. J. 1995, *A&AS*, **113**, 409
- Suganuma, M., Yoshi, Y., Kobayashi, Y., et al. 2006, *ApJ*, **639**, 46
- Sulentic, J. W., Marziani, P., Zamanov, R., et al. 2002, *ApJL*, **566**, L71
- Svensson, R., & Zdziarski, A. A. 1994, *ApJ*, **436**, 599
- Tody, D. 1986, *Proc. SPIE*, **627**, 733
- Urry, C. M., & Padovani, P. 1995, *PASP*, **107**, 803
- Vanden Berk, D. E., Shen, J., Yip, C.-W., et al. 2006, *AJ*, **131**, 84
- Viner, M. R., & Erickson, W. C. 1975, *AJ*, **80**, 931
- Waldram, E. M., Yates, J. A., Riley, J. M., & Warner, P. J. 1996, *MNRAS*, **282**, 779
- Westhues, C., Haas, M., Barthel, P., et al. 2016, *AJ*, **151**, 120
- Wilkes, B., Lal, D. V., Worrall, D. M., et al. 2012, *ApJ*, **745**, 84
- Wilkes, B. J., Kuraszkiewicz, J., Haas, M., et al. 2013, *ApJ*, **773**, 15
- Willott, C. J., Martínez-Sansigre, A., & Rawlings, S. 2007, *AJ*, **133**, 564
- Willott, C. J., Rawlings, S., Archibald, E. N., & Dunlop, J. S. 2002, *MNRAS*, **331**, 435
- Willott, C. J., Rawlings, S., Blundell, K. M., & Lacy, M. 2000, *MNRAS*, **316**, 449
- Wills, B. J. 1975, *AuJPA*, **38**, 1
- Wright, A., & Otrupcek, R. 1990, *PKS Catalog*, 0
- Wright, E. L. 2006, *PASP*, **118**, 1711
- Zhang, S. N., Cui, W., & Chen, W. 1997, *ApJL*, **482**, L155
- Zhu, S. F., Brandt, W. N., Luo, B., et al. 2020, *MNRAS*, **496**, 245